TDP-43 dysfunction leads to impaired proteostasis and predisposes mice to worse neurological outcomes after brain injury

Melissa S. Rotunno [1,2], Megan Fowler-Magaw [1,3,#], Jianjun Zhong [1,4,#], Kennedy O'Hara [1,3], Elenore A. Wiggin [1,5], Debra Cameron [1], Karly Stallworth [1,2], James Bouley [1], Holly McEachern [6,7], Mina N. Anadolu [8], Jeffrey A. Nickerson [9], Andrew R. Tapper [10], Susanna Molas [10], Francesca Massi [2,11], Nils Henninger [1,3,12], Oliver D. King [1,3], Daryl A. Bosco [1,2,3,5,11,13*]

[1]Department of Neurology, University of Massachusetts Chan Medical School, Worcester, Massachusetts, MA, 01605

[2]Department of Biochemistry and Molecular Biotechnology, University of Massachusetts Chan Medical School, Worcester, MA, 01605

[3]Neuroscience Program, Morningside Graduate School of Biomedical Sciences, University of Massachusetts Chan Medical School, Worcester, MA, 01605

[4]Department of Neurosurgery, The First Affiliated Hospital of Chongqing Medical University, Chongqing, China, 400016.

[5]Interdisciplinary Graduate Program, Morningside Graduate School of Biomedical Sciences, University of Massachusetts Chan Medical School, Worcester, MA, 01605

[6]RNA Therapeutics Institute, UMass Chan Medical School, Worcester, MA, 01605

[7]RNA Therapeutics and Biology Program, Morningside Graduate School of Biomedical Sciences, University of Massachusetts Chan Medical School, Worcester, MA, 01605

[8]Program in Molecular Medicine, University of Massachusetts Chan Medical School, Worcester, MA, 01605

[9]Department of Pediatrics, University of Massachusetts Medical School, Worcester, Worcester, MA, 01605

[10]Department of Neurobiology, Brudnick Neuropsychiatric Research Institute, University of Massachusetts Chan Medical School, Worcester, MA, 01605

[11]Biochemistry and Molecular Biotechnology Program, Morningside Graduate School of Biomedical Sciences, University of Massachusetts Chan Medical School, Worcester, MA, 01605

[12]Department of Psychiatry, University of Massachusetts Chan Medical School, Worcester, MA

[13]Lead Contact

[#]These authors contributed equally

*To whom correspondence should be addressed: Daryl A. Bosco: Department of Neurology, University of Massachusetts Chan Medical School, Worcester, MA 01605; Daryl.Bosco@umassmed.edu; Tel. (774) 455-3745; Fax. (508) 856-6750

ABSTRACT

Background: Pathological TAR DNA-binding protein 43 (TDP-43) dysfunction is associated with multiple neurodegenerative disorders. However, the mechanistic link between TDP-43 dysfunction and neurodegeneration is poorly understood and likely involves a combination of genetic and environmental risk factors. A major risk factor for neurodegenerative disease is exposure to traumatic brain injury (TBI). Here, we investigated the synergistic interplay between TDP-43 dysfunction and TBI in a murine model of amyotrophic lateral sclerosis (ALS)/ frontotemporal dementia (FTD).

Methods: A model of TDP-43 dysfunction caused by a knock-in Q331K mutation in *Tardbp* was combined with a mild model of TBI. Control conditions included both WT mice and mice with sham surgery. Animals were evaluated for behavioral deficits at timepoints pre- and post-surgery. Additionally, post-mortem brain tissues were examined using RNA sequencing and mass spectrometry-based quantitative proteomics together with histological and biochemical analyses.

Results: Expression of dysfunctional TDP-43 *in vivo* caused deficits in multiple branches of the proteostasis network, including protein folding, protein synthesis, and protein turnover. Examples include mis-expression of chaperones and genes within the ubiquitin-proteosome pathway in mutant TDP-43 versus WT mice. Further, mutant TDP-43 expression correlated with reduced thermostability of proteins associated with the ribosome and the chaperonin containing TCP-1 complex. In response to TBI, mutant TDP-43 mice exhibited significantly worse neurological outcomes relative to WT animals. Heightened neurological deficits in mutant TDP-43 mice following TBI coincided with a robust upregulation of proteostasis- and stress-related genes at the transcript level. However, this upregulation was not detected at the protein level.

Conclusions: Our data demonstrate that expression of dysfunctional TDP-43 leads to deficits within the proteostasis network in vivo at baseline. Despite an upregulation of proteostasis-related genes at the transcript level in mutant TDP-43 mice after TBI, mutant TDP-43 mice exhibit an impaired response to, and recovery from, brain trauma relative to their WT counterparts. Restoring proteostasis is expected to protect against the detrimental effects of TDP-43 dysfunction, especially under stress conditions that promote neurodegenerative disease.

Keywords: TDP-43, traumatic brain injury, proteostasis, ribosome, Proteome Integral Solubility Alteration (PISA), multistep hypothesis, amyotrophic lateral sclerosis, frontotemporal dementia, mass spectrometry, transcriptomics.

BACKGROUND

TAR DNA-binding protein 43 (TDP-43) is an essential RNA/DNA-binding protein that performs critical functions in the context of RNA splicing, transport, and expression.(1) TDP-43 shuttles between the nucleus and cytoplasm while fulfilling these functions, although the protein is predominately expressed in the nucleus under physiological conditions. A significant cytoplasmic shift in TDP-43 localization has been observed in cultured cells exposed to various external stimuli

73 or “stressors” that inhibit proteasomal and transcriptional activity, or that induce hyperosmolarity,
74 hyperexcitability or excitotoxicity.(2-6) While the mechanisms underlying stress-induced
75 cytoplasmic accumulation of TDP-43 have not been fully elucidated, recent reports have shown
76 that both RNA binding capacity and post-translational modification of TDP-43 affect TDP-43
77 subcellular localization.(3, 7-10) TDP-43 has also been identified as a component of cytoplasmic
78 condensates called stress granules, which form in response to acute cellular stress.(11-13)
79 Autosomal dominant mutations in TDP-43 that cause familial amyotrophic lateral sclerosis (ALS)
80 alter the properties of stress granules as well as other TDP-43-associated ribonucleoprotein
81 (RNP) granules,(10-12, 14-16) possibly through altered phase separation behavior of mutant
82 TDP-43 with itself, other RNA-binding proteins and/or RNA.(10, 17-20) Collectively, these
83 observations indicate that subcellular TDP-43 localization can serve as a proxy for cellular stress.
84 Further, the effects of TDP-43 on stress response pathways can be perturbed by disease-causing
85 mutations.
86
87 In addition to TDP-43 mutations in familial ALS, TDP-43 has emerged as a hallmark pathological
88 feature across multiple neurodegenerative disorders termed TDP-43 proteinopathies,(21)
89 including ALS, frontotemporal lobar degeneration (FTLD),(22, 23) Alzheimer’s disease (AD),(24)
90 limbic-predominant age-related TDP-43 encephalopathy (LATE)(25) and chronic traumatic
91 encephalopathy (CTE).(26). Cells with cytoplasmic accumulation and/or nuclear depletion of
92 TDP-43 have been shown to exhibit splicing defects that are consistent with TDP-43 loss-of-
93 function in human post-mortem CNS tissues from ALS/FTLD and AD cases.(4, 27-31) Most cases
94 of human TDP-43 proteinopathy occur sporadically with poorly defined etiologies, and likely
95 develop through a combination of genetic susceptibility and environmental risk factors.(32, 33)
96 Indeed, emerging evidence supports that ALS pathogenesis occurs through a multistep process,
97 even in cases with penetrant genetic mutations in *TARDBP* encoding TDP-43.(34) The multistep
98 hypothesis purports that individual ALS-linked mutations cannot fully account for the disease

99 process, which must include other factors such as additional genetic mutations, environmental
100 exposures and/or physical stress.(34, 35)

101 Traumatic brain injury (TBI) is a form of physical stress that also represents a major risk factor for
102 developing neurodegenerative diseases, including those with TDP-43 pathology.(36) Cytoplasmic
103 shifts in TDP-43 localization have been reported in laboratory animal models of TBI.(13, 37-41)
104 Further, recurrent TBI leads to CTE with cytoplasmic TDP-43 pathology in humans.(26, 42) Here,
105 we sought to investigate the relationship between stress and TDP-43 dysfunction in the context
106 of a multistep model of neurodegenerative disease. To this end, we combined a murine model of
107 TDP-43 dysfunction caused by a genetic knock-in mutation in *Tardbp* together with a mild model
108 of TBI.(43, 44) Our results revealed that mutant TDP-43 mice exhibit significantly worse
109 neurological outcomes during the acute phase post-TBI relative to their wild-type (WT)
110 counterparts. Corresponding transcriptomics and RT-PCR analyses revealed synergistic effects
111 of TDP-43 mutation and TBI on gene expression and processing. For example, a significant
112 upregulation of proteostasis- and stress-related genes was detected specifically in brain tissue
113 from mutant TDP-43 mice after TBI. Many of the pathways that became upregulated in mutant
114 TDP-43 mice following TBI were also highlighted in a recent transcriptomics analysis of post-
115 mortem ALS and FTLD-TDP CNS tissues.(45, 46) While this TBI model caused a cytoplasmic
116 shift in TDP-43 localization, this change in TDP-43 localization did not appear to correlate with
117 mis-splicing events caused by TDP-43 loss-of-function. Rather, we found that mutant TDP-43
118 expression correlated with reduced thermostability of cytoplasmic ribosomal proteins. In fact,
119 diminished thermostability of ribosomal proteins correlated with mutant TDP-43 expression,
120 irrespective of whether mutant TDP-43 mice had been exposed to brain trauma or not. Notably,
121 TDP-43 has been shown to associate with ribosomes and to modulate both global and local
122 translation.(47-50)

123 The outcomes of this study are consistent with a model in which expression of mutant TDP-43
124 leads to deficits throughout the proteostasis network. Upon CNS challenge, compensatory
125 mechanisms appear to become activated in mutant TDP-43 mice, yet these mice fail to mount
126 the physiological response to brain injury exhibited by their WT counterparts. Therefore, our data
127 demonstrate that expression of dysfunctional TDP-43 leads to impaired response to, and recovery
128 from, brain trauma and provide mechanistic insight into TBI as a risk factor for TDP-43
129 proteinopathies. Restoring proteostasis may therefore protect against the effects of TDP-43
130 dysfunction, especially under conditions of CNS challenge that promote neurodegenerative
131 disease.

132 **METHODS**

133 **Animals**

134 All animal related protocols were conducted in accordance with the Guide for the Care and Use
135 of Laboratory Animals published by the National Research Council (US) Committee. The
136 protocols were approved by the Institutional Animal Care and Use Committee (IACUC) of the
137 University of Massachusetts Chan Medical School. Mice with the human-equivalent TDP-43
138 Q331K mutation on a pure C57BL/6J (WT) background were generated and characterized in a
139 previous study.(44) All experiments herein were performed with aged-matched, male mice with
140 either the homozygous TDP-43 Q331K or TDP-43 WT genotype. Mice were generated using
141 standard breeding approaches or via *in vitro* fertilization at the UMass Chan Medical School
142 Transgenic Animal Modeling Core (TAMC; Worcester, MA). All mice were maintained under
143 standard conditions with no more than 5 mice per cage, on a standard 12h light/dark cycle (white
144 light ON at 7:00am and OFF at 7pm), and were provided *ad libitum* access to food and water.

145 **Traumatic brain injury (TBI) surgery**

146 Mice at 16-weeks of age were exposed to TBI or sham surgery. TBI surgeries were based on a
147 previously published protocol.(43) Details of the TBI surgery used herein were published by us

148 elsewhere.(51) Briefly, mice were anesthetized with 3% isoflurane (Pivetal, NDC 46066-755-03)
149 in carrier gas at 1.5 L/min flow. Prior to surgery, buprenorphine (PAR Pharmaceutical, NDC
150 42023-179-05) was administered subcutaneously at 1 mg/kg. Hair was removed from the top of
151 the head and the scalp skin was disinfected with 75% ethanol and betadine. A ~1.2-1.5 cm
152 incision was made along the midline starting approximately 3 mm posterior from the eyes to
153 expose the right parietal skull. The skin over the left and right hemispheres of the skull was
154 excised. The periosteum was removed and the exposed skull was positioned on a cushion
155 beneath the weight-drop. A transducer rod tip was aligned to the skull-top location: 2.5 mm
156 posterior to Bregma and 2 mm lateral to the midline. From a height of 15 cm, a 50-gram
157 weight was released that came into contact with a transducer, which in turn delivered an impact
158 onto the mouse's intact skull (see diagram in **Fig. 1A**). After the impact, mice were placed onto a
159 heating blanket in a supine position for the time needed to wake from the anesthesia (i.e., time
160 required to right themselves to a prone position), which took on the order of minutes for each
161 mouse. Mice were then returned to the anesthesia chamber in preparation for a subsequent
162 impact; this process was repeated a total of ten times within a single surgical session. As the
163 impacts were delivered within the same surgical session and not spaced by days or weeks, this
164 model is not considered a repetitive TBI model that we described previously.(40, 52) After the
165 surgery was completed, cefazolin (HIKMA Pharmaceutical, NDC 0143-9924-90) was
166 administered intramuscularly at 500 mg/kg and meloxicam (Norbrook, NDC 55529-040-10) was
167 administered subcutaneously at 5 mg/kg. Mice were placed on a heating blanket and monitored
168 until they were ambulatory (approximately 15 minutes), and then transferred to their home cage.
169 Buprenorphine was administered as described above at 8 h, 16 h and 24 h after the first dose.
170 For the sham surgery, mice underwent the same procedure as the TBI mice but without the
171 weight-drop impact.

172 **Neurological Severity Score (NSS) Test**

173 The NSS test was performed at 12 time points: pre-surgery and 2h, 24h, 48h, 1 week, 2 weeks,
174 3 weeks, 4 weeks, 8 weeks, 12 weeks, 16 weeks and 20 weeks post-surgery, as previously
175 described in detail.(43, 53) Body weight was measured prior to every NSS testing session. Briefly,
176 the NSS consists of 10 individual tasks designed to assess motor function, alertness and
177 physiological behavior. Each task was completed regardless of whether the mouse passed or
178 failed previous tasks. For each task, mice were assigned a score of 1 to indicate failure of the
179 task or 0 if the task was completed, resulting scores ranging between 0 (no deficit) and 10
180 (maximum deficit). The NSS test was performed by a lab technician who was blinded to the
181 genotype and surgery type of the mice. For statistical analyses, between-group comparisons of
182 the NSS over repeated measurements (time) were conducted using longitudinal mixed models.
183 Time was treated as a categorical variable. The models included group (each group representing
184 both a genotype and surgery type) and time as fixed covariates, as well as the two-way interaction.
185 When the main effects were significant, pairwise comparisons were conducted to identify
186 significance by group and time point. A two-sided $p<0.05$ was considered statistically significant.
187 Statistical analyses were performed using SPSS Statistics Version 29 (IBM-Armonk, NY).

188 **Cued and Contextual Fear Conditioning (CCFC) Test**

189 Animals were generated through two in vitro fertilization procedures at the Transgenic Animal
190 Modeling Core (TAMC) at UMass Chan Medical School using heterozygous Q331K male and
191 female mice. Homozygous Q331K and WT mice were randomly assigned to group 1 or group 2,
192 and both groups were subjected to the CCFC test before surgery. The CCFC test was conducted
193 at the UMass Chan Mouse Behavioral Core facility using the EthoVision XT system (Noldus,
194 BOM-EV-0001). Mice were placed in a Ugo Basile Fear Conditioning Chamber (Noldus, BOM-
195 XUGO-F101) made of optical transparent plastic 26 cm long, 26 cm wide and 38 cm tall. The top
196 of the chamber was equipped with a monochrome GigE camera (Noldus, BOM-XCAM-GIGE)
197 used to track animal movement in real-time during the testing session. The bottom of the chamber

contained electricity-conductive metal strips to deliver foot shocks. The chamber was nested in a cabinet equipped with a speaker to deliver white noise and high-frequency tones per the experimental design detailed below. The cabinet wall was insulated to reduce environmental noise and a built-in ventilator allowed for air-exchange. All the inputs, including white noise, tone, and foot shock, were controlled with a computer-based operation console (Ugo Basile, version 1.1.8.9). EthoVision XT 15 software was used for animal tracking and data analysis. The live tracking started immediately when the animal entered the chamber, after which there was a 60s delay prior to the start of an input. The full test session was conducted over four consecutive days as follows. Note that the white noise and the tone input were delivered randomly, with random intervals (ranging from 5s to 30s) between these two inputs for all tests on each day.

Day 1:

White noise: 50% intensity, 30s duration, and repeated 5 times.

Tone: 1000 Hz, 50% intensity, 30s duration, and repeated 5 times.

Day 2:

White noise: 50% intensity, 30s duration, and repeated 5 times.

Tone: 1000 Hz, 50% intensity, 30s duration, and repeated 5 times.

Electrical foot shock: 0.75 mA intensity that occurred at the last second of each tone. Each mouse received five foot shocks in total on Day 2 with each shock lasting for 1s.

Day 3:

White noise: 50% intensity, 30s duration, and repeated 5 times.

Tone: 1000 Hz, 50% intensity, 30s duration, and repeated 5 times.

Novel context: To create a novel context, a new scent and visual component were introduced to the chamber as follows. One drop of vanilla extract (novel scent) was applied to a piece of tissue paper, which was placed in the feces tray underneath the chamber. Paper boards with white and black stripes (novel visual) were attached to the outer side of the chamber.

Day 4:

224 The context was reverted as per Days 1 and 2 (i.e., the paper boards were removed and the feces
225 tray cleaned before Day 4) for testing on Day 4.
226 Neither white noise nor tone were implemented.
227 Below is a table summarizing the inputs and contexts for the CCFC test:

	Day 1	Day 2	Day 3	Day 4
White noise	+	+	+	-
Tone	+	+	+	-
Foot shock	-	+	-	-
Novel context	-	-	+	-

228 For analysis of Days 1-3, the initial 29s of each input was extracted to avoid potential interference
229 from the last second when the foot shock was delivered. Therefore, the total duration for white
230 noise and tone inputs is 29s x 5 = 145s. For Day 4, the consecutive 145s after the initial 60s delay
231 was extracted for the analysis. Mouse movement was detected by the software at the pixel level
232 for the entire chamber from one video frame to the next. Thresholds based on animal activity
233 within the chamber were set as follows: immobility state (<0.1% pixel change in the chamber),
234 movement between immobility and walking (between 0.1% and 0.5%) and walking (>0.5%). The
235 amount of time animals spent in an immobility state was interpreted as freezing behavior and
236 plotted for each day (Day 1-4). The statistical analysis was performed as described above for
237 NSS, where between-group comparisons over repeated measurements (time) were conducted
238 using longitudinal mixed models. Time was treated as a categorical variable. The models included
239 group and time as fixed covariates, as well as the two-way interaction. When the main effects
240 were significant, pairwise comparisons were conducted to identify significance by group and time
241 point. A two-sided $p<0.05$ was considered statistically significant. Statistical analyses were
242 performed using SPSS Statistics Version 29 (IBM-Armonk, NY).

243 **RNA isolation**

244 Mouse brain tissue samples (~40 mg and 4 mm of diameter) were collected from the impact site
245 (**Fig. 1A**) and the corresponding site on the contralateral side using a sterile disposable biopsy
246 punch (Integra Miltex, 33-32) that excised tissue from the brain surface (i.e., cortex) to the brain
247 bottom (i.e., hypothalamus). Total RNA was isolated from mouse brain tissues using Qiagen's
248 RNeasy Lipid Tissue Mini Kit (Cat. No. 74804) with DNase treatment following the manufacturer's
249 protocols. RNA concentration and absorbance were measured by a Nanodrop device (ND1000).
250 Samples with A260/A280 between 1.8 to 2.2 were considered suitable for downstream
251 applications.
252
253 **Transcriptome analysis by RNA-sequencing (RNAseq)**
254 For the 24h-post TBI timepoint, RNAseq analysis was performed on RNA isolated from brain
255 tissue as described above for six groups of mice: homozygous Q331K and WT genotypes, each
256 under naïve, sham, and TBI conditions. For the 7mo-post TBI timepoint, only sham and TBI
257 conditions for homozygous Q331K and WT genotypes were included. Sham and TBI conditions
258 are described under TBI surgery. Naïve mice were not subjected to surgery and are therefore
259 treated a separate control group than sham surgery mice. Between 3-6 mice were included per
260 group for a total of 46 samples. RNA quality assessment, library preparation and sequencing were
261 conducted by Novogene Co., LTD (Beijing, China). Poly-T oligo-attached magnetic beads were
262 used for poly-A capture, random hexamer primers for first strand cDNA synthesis, and dTTP for
263 second strand cDNA synthesis of non-directional libraries. Libraries were sequenced to a depth
264 of 50M-125M raw read pairs (2x150 PE) per sample using an Illumina NovaSeq 6000 sequencer.
265 After trimming adapter sequences and low-quality bases, reads were mapped with HISAT2
266 (2.0.5)(54) to the mouse mm39 reference genome with Ensembl release 107 gene annotations.
267 Two samples (one Q331K sham and one Q331K TBI) from the 24h post-TBI timepoint were
268 excluded from further analyses, as they were strong outliers in Principal Component Analysis
269 (PCA) of expression values (counts-per-million on $\log_2$ scale with prior.count=1; **Fig. S1A**); see

270 **Additional File 1** for all supplemental figures. These samples were also outliers for several
271 mapping quality control (QC) metrics, with higher-than-usual fractions of multi-mapping, exonic,
272 and unspliced reads. Two samples (one Q331K sham and one WT TBI) were also excluded from
273 the 7mo-post TBI dataset because they were determined to by outliers in the PCA analysis (**Fig.**
274 **S1B**).
275
276 Differential gene expression analyses were performed in R (4.3.2) using quasi-likelihood methods
277 in the edgeR package (4.0.12).(55) Data from 24hr-post TBI and 7mo-post TBI experiments were
278 analyzed separately. The TMM method was used for computing normalized library sizes and
279 genes with low counts were filtered out in preprocessing. For both datasets, ~25,000 genes were
280 retained with at least 5 scaled counts in at least 3 samples, where the scaling adjusts for
281 differences in total library sizes (read counts across all genes) between samples while keeping
282 the median library size unchanged. The function glmQLFit (with non-default options robust=T
283 and prior.count=1) was used to fit the expression data with a design matrix that included factors
284 for injury (INJ, with levels Naïve, Sham, and TBI), genotype (GT, with levels Q331K and WT) and
285 their interaction (model formula ~0 + GT:INJ). Differential expression was assessed using the
286 function glmQLFTest for contrasts that included nine simple between-group comparisons
287 (WT.TBI vs WT.Sham, etc.); main effects of GT (Q331K vs WT) and INJ (TBI vs Sham), though
288 in both cases excluding the groups with INJ=Naïve; and a test for an interaction between GT and
289 INJ, again excluding the groups with INJ=Naïve. For the 7mo-post TBI data the naïve mice were
290 not included, and the model also included an additive factor for IVF batch (with two levels, 162
291 and 167). Supplemental Table I includes the $\log_2$(fold-change) [LFC], p-value, and FDR for each
292 gene for each contrast discussed in the results section.
293
294 Gene Set Enrichment Analysis (GSEA, 4.3.3) was performed using the Hallmark
295 (mh.all.v2024.1.Mm.symbols.gmt) and Gene Ontology Biological Process (GOBP,

296 m5.go.bp.v2024.1.Mm.symbols.gmt) gene set collections from the Molecular Signatures
297 Database (MSigDB).(56-60) Cutoffs on Normalized Enrichment Score (NES) and adjusted p-
298 value (FDR) were used to determine significantly altered gene sets (|NES| > 1.5 and FDR<0.05).
299 NES is a score that reflects the overrepresentation of a gene set at the upper (positive value) or
300 lower (negative value) end of a ranked gene list, after normalization to account for variation in
301 gene set size. The gene list was pre-ranked based on directional p-values for the indicated
302 comparison ($-\log_{10}$(p-value)*sign of $\log_2$(fold change)). A weighted enrichment statistic was used
303 in the analysis. The 10 top gene sets based on highest |NES| are displayed for all enrichment
304 analyses. If fewer than 10 are displayed then all gene sets that meet the cutoff criteria are shown.
305 All gene set hits that meet the cutoff criteria can be found in **Supplemental Table II**.
306
307 **Quantitative Proteomics**
308 Mice were perfused with PBS prior to tissue isolation for all proteomic analyses. Mouse brain
309 tissue samples were collected as described above under RNA isolation and cut into ~1 mm
310 diameter pieces. For whole brain proteomics, the tissue was transferred to a pre-cooled glass
311 homogenizer on ice with 900 µl of RIPA buffer (Sigma-Aldrich R0278-50ML) containing 1x
312 protease inhibitor (Roche, 11873580001) and 1x phosphatase inhibitor (Roche, 04906837001).
313 Complete tissue homogenization was performed with a WHEATON Power Homogenizer and
314 Overhead Stirrer (catalog number 903475, serial number G082210) by setting the stirring speed
315 on level 2 for 1 minute. The sample was transferred to a plastic tube together with 300ul of RIPA
316 buffer that was added to rinse the homogenizer. The sample was left on ice for 30 min and then
317 centrifuged at 15,899 xg for 10 min at 4°C in a table-top centrifuge (AXYGEN, serial number
318 LRMPL1-1710018, lot number 04619100). The supernatant was transferred into a fresh tube and
319 the bicinchoninic acid (BCA) assay (Thermo Scientific, 23223) was used to measure the protein
320 concentration. For cytoplasmic samples depleted of nuclei and mitochondria for PISA (below),
321 samples were homogenized in 1.1 mL of KPBS (130 mM KCl, 10 mM KH_2PO_4, pH 7.3). Minced

322 tissue was homogenized twice on level 2 for 1 min each with 1 min on ice in between.
323 Homogenate was transferred to a 1.5 ml Eppendorf tube. The glass tube was rinsed with 0.3 ml
324 of KPBS +PI and added to a 1.5 ml Eppendorf tube. Samples were spun twice at 600 xg at 4°C
325 for 5 min with supernatant moved to a fresh Eppendorf tube each time to remove the nuclear
326 fraction and debris. Samples were then centrifuged at 7,000 xg at 4°C for 10 min to remove
327 mitochondria.

328 For PISA analysis, cytoplasmic samples depleted of nuclei and mitochondria were diluted in half
329 to 1 mg/ml with PISA lysis buffer (2 mM MgCl2, 1% CA630, PBS (Corning 21-031-CV)). Lysates
330 were incubated on ice for 30 min and subdivided into 4 aliquots in PCR strip tubes. One aliquot
331 was kept on ice to use for the total protein level quantitative proteomics. The remaining three
332 aliquots were exposed to a single temperature (52°C, 53°C, 54°C) for 3 min followed by
333 equilibration to 25°C for 5 min. The three temperatures (52°C, 53°C, 54°C) for each sample were
334 combined and centrifuged at 20,817 xg for 99 min at 4°C to remove aggregated protein.
335 Supernatant (soluble fraction) was moved to a new tube. All samples were frozen on dry ice and
336 dried down in speedvac (**Fig. S10A**).

337 For tandem mass tag (TMT) proteomics, 50 μg of protein (whole brain) or 12 μg (organelle
338 depleted cytoplasm) was dried down in a speedvac (Thermo Scientific, SPD111V), resuspended
339 in 23 μl of 1x lysis buffer (5% SDS, 50 mM TEAB, pH8.5) and digested with Trypsin/LysC (Thermo
340 Scientific, A41007) using S-Trap micro columns (ProtiFi, C02-micro-80) as described by the
341 manufacturer. Eluted peptides were dried in a speedvac and resuspended in 20 μl (whole brain)
342 or 5 μl (organelle depleted cytoplasm) of 100 mM TEAB pH 8.5. The resuspended peptides were
343 added to a tube containing TMT tag for a final protein:TMT ratio of 1:2 (ThermoFisher, #A44521).
344 The reaction was quenched with 0.5 μl of 5% hydroxylamine and incubated for 15 min at 25°C
345 with shaking (300 rpm). Quenched samples were combined and dried down in aliquots with 50

346 μg set aside as “pre-fractionation” sample. For fractionation (whole brain only), 125 μg aliquot
347 was resuspended in 300 μl of 0.1% TFA and sonicated for 5 min. The sample was subjected to a
348 high pH reversed phase fractionation procedure as described by manufacturer (Pierce,
349 #84868). Fractions 2 and 8 were combined and dried down. Fractions 3-7 were kept separate
350 and dried down. Fractions and input samples were reconstituted with 20 μl of 5% acetonitrile,
351 0.1% formic acid and 3.8 μl was injected per replicate.

352 Liquid chromatography tandem mass spectrometry (LC–MS/MS) experiments were performed in
353 duplicate for fractionated samples and in triplicate for unfractionated samples. Samples were run
354 in a 145 min gradient from 10% of acetonitrile (0.1% formic acid) to 70% acetonitrile, 0.1% formic
355 acid in data dependent mode on a nanoACQUITY UltraPerformance LC (UPLC; Waters, Milford,
356 MA, USA) coupled to an Orbitrap Fusion Lumos Tribid mass spectrometer. MS data acquisition
357 was collected from 400 to 1400 m/z with a resolution of 120,000. MS2 Data Dependent Acquisition
358 was acquired with a resolution of 50000 at m/z 200 with a mass injection time of 120 ms. Other
359 acquisition methods and column setup were identical to those described previously.(61) Raw
360 data files were processed with MaxQuant version 2.4.11.0. with reviewed entries only of mouse
361 uniprotKB FASTA file (downloaded 08/09/2023) to identify peptide-spectrum matches (PSM) and
362 to consolidate replicate injections.(62) Search parameters included Trypsin/P enzyme, fixed
363 modification of carbamidomethylation on cysteine (+57 on C) and variable modifications of
364 oxidized methionine (+16 on M), phosphorylation of serine (S), threonine (T), and tyrosine (Y)
365 (+80 on STY) and N-terminal acetylation (+42). The files were processed with Reporter MS2 type
366 set to TMT 16-plex (+304 on peptide N-Terminal and Lysine). Assignments were made using a
367 20-ppm mass tolerance for first search and 4.5 for main search for the precursor and 0.5 Da mass
368 tolerance for the fragments with a 1% FDR set for PSM and Protein. The proteinGroups output
369 text file was imported into Perseus (2.0.10.0) for $\log_2$ transformation, imputation using values
370 based on normal distribution, and quantile normalization.(63) Additional filters included numerical

371 value in at least 4 of the 16 samples and 2 unique peptides for protein identification. The exported
372 table was then processed in RStudio (R version 4.3.3) using limma (3.58.1) for differential
373 expression (or stability) testing with a linear model that had a factor for group, whose levels were
374 the four combinations of GT (Q331K or WT) and INJ (TBI or Sham). Empirical Bayes moderated
375 t-statistics were computed for contrasts that included four between-group comparisons (WT.TBI
376 vs WT.Sham, Q331K.TBI vs Q331K.Sham, WT.TBI vs Q331K.TBI, and WT.Sham vs
377 Q331K.Sham), main effects of GT (Q331K vs WT) and INJ (TBI vs Sham), and the interaction
378 between GT and INJ. Proteins with an FDR < 0.1 were considered significantly different for these
379 contrasts. For the PISA data processing, one Q331K sham sample was identified as an outlier
380 based on total intensity and excluded from further analyses. Data are available via
381 ProteomeXchange with identifier PXD068825 and 10.6019/PXD068825.

382 **Western blotting**

383 For Western blot analyses, protein samples were mixed with loading buffer (Boston BioProducts,
384 BP-111R) and boiled at 100 °C for 5 min. Gel electrophoresis was performed with the BIO-RAD
385 PowerPac HC followed by a transfer onto polyvinylidene fluoride (PVDF; Merck Millipore,
386 IPFL00010) membrane. The PVDF membrane was blocked for 1h at ambient temperature using
387 Intercept Blocking Buffer (LI-COR, 927-70003) and then primary antibody (see table below) was
388 incubated at 4°C overnight (>12 h) in PBST and secondary antibody was incubated at ambient
389 temperature for 1 h in blocking buffer. The PVDF membrane was imaged using the LI-COR
390 ODYSSEY infrared imager system (Serial No. ODY-2215). The target protein intensity was
391 quantified using Image Studio software (Lite Ver 5.2).

392

393

394

Antibody	Manufacturer	Catalog #	Dilution
H3	Proteintech	17168-1-AP	1:1000
Calr	Enzo life sciences	ADI-SPA-602	1:1000
Cox4	Abcam	AB14744-1005	1:1500
GAPDH	Sigma-Aldrich	G8795	1:2000
Rpl4	Proteintech	11302-1-AP	1:2000
Rps6	Cell Signaling	2217	1:500
TDP43	Encor	MCA3H8	1:5000
Anti-Mouse IgG 680	LICORbio	926-68072	1:10,000
Anti-Rabbit IgG 800	LICORbio	926-32211	1:10,000

395

396 **Immunostaining**

397 Mice were euthanized and transcardially perfused with PBS and 4% paraformaldehyde (PFA;
398 Fisher Scientific, AAA1131336) in 1X PBS, pH 7.4. Mice were decapitated, and the scalp and
399 skull carefully removed to harvest the intact brain. All brain samples were immersed in 4% PFA
400 solution for 24h at 4°C for post-fixation. A brain matrix (CellPoint Scientific, Alto Acrylic 1mm
401 Mouse Brain Coronal) was used to pre-section the brains into anterior, medial, posterior and
402 cerebellar sections, which were embedded in paraffin by the Morphology Core (UMass Chan
403 Medical School). Coronal sections of 7 μm thickness were prepared on a Leica RM2125 RTS and
404 mounted onto charged microscope slides (Globe Scientific Cat#1354W). Prior to immunostaining,
405 tissues were deparaffinized with xylenes (Fisher Scientific, X3P-1GAL) and rehydrated in 100%
406 and 70% ethanol (Fisher Scientific, 04355223EA). Tissues were subjected to antigen retrieval
407 using 10mM Sodium Citrate (Fisher Scientific, S25545) containing 0.05% Tween 20 (Fisher
408 Scientific, BP337-500) at pH 6.0, heated to boiling, and then maintained at 95°C in a steamer
409 (Black&Decker Cat# HS1050) for 30 minutes. Tissues were blocked using 1% bovine serum
410 albumin (BSA; Fisher Scientific, BP1600-100) and 3% horse serum (Gibco, 26050-070) in PBS
411 for 1h at ambient temperature. Tissues were probed with rabbit anti-TDP-43 (1:250 Proteintech,
412 10782-2-AP) and chicken anti-NeuN (Millipore Sigma, ABN91) antibodies at 4°C overnight.
413 Tissues were incubated at ambient temperature for 1h with fluorophore-conjugated secondary
414 antibodies (Jackson ImmunoResearch Laboratories) at 1:500 and counterstained with DAPI.

415 Prolong Gold antifade reagent (Invitrogen, P36930) with a refractive index of 1.46 was used to
416 mount coverslips onto the tissues.

417 **Confocal Microscopy**

418 TDP-43/NeuN/DAPI immunofluorescence images were obtained using a Leica TCS SP5II (S/N:
419 5100001537, 11888906 BZ:01) confocal microscope. A 40x objective lens with oil was used to
420 acquire images. Leica Application Suite Advanced Fluorescence (LAS AF) software was used for
421 image acquisition as follows: imaging mode: XYZ; Sequential imaging: on; Format: 512x512;
422 Pinhole: on; Speed: 400 Hz; Line average: 1; Frame average: 3, Accu for Line average: 1; Accu
423 for Frame average: 1; Z-stack mode: Z-wide; Sequential scan mode: between frames, number of
424 steps: 3; Z-step size: ~0.5 µm. Using these settings, images were collected in the following order:
425 ipsilateral cortex, ipsilateral amygdala, ipsilateral hypothalamus, contralateral hypothalamus,
426 contralateral amygdala and contralateral cortex.

427 **TDP-43 localization analyses**

428 TDP-43 nuclear-to-cytoplasmic (N/C) ratio analysis was performed with 40x confocal images
429 described above on a per image basis with a custom macro generated with Fiji (**Additional file**
430 **2).** (64) DAPI signal was used to define the area of nuclear TDP-43 fluorescence and the
431 cytoplasm was defined as any area outside of the DAPI-defined region. Mean TDP-43
432 fluorescence intensity was measured for the nuclear and cytoplasmic regions, and the N/C ratio
433 was calculated by dividing the mean nuclear TDP-43 signal by the mean cytoplasmic TDP-43
434 signal.

435 TDP-43 N/C ratio analysis was also performed on a per-cell basis using a customized pipeline
436 that was developed in CellProfiler(65) for calculation of the percentage of cells with increased
437 cytoplasmic TDP-43 **(Additional file 3)**. DAPI signal was used to identify the nuclear region,
438 which was then expanded by 8 pixels to capture a contiguous cytoplasmic region. The mean TDP-
439 43 fluorescence intensity was measured for the defined nuclear and cytoplasmic regions and the

440 N/C ratio was calculated as described above for the per image analysis. Cells with an N/C ratio
441 <5.72 were classified as having cytoplasmic TDP-43. This threshold was determined using the
442 average N/C ratio of each field of view (FOV) in the WT sham condition (representing a condition
443 that did not exhibit robust cytoplasmic TDP-43) minus one standard deviation. Within a FOV, the
444 number of cells with an N/C ratio <5.72 was then divided by the total number of cells, multiplied
445 by 100 to obtain the percentage cells with cytoplasmic TDP-43 for each condition.
446
447 The CellProfiler pipeline above was also used to measure the distribution of TDP-43 signal within
448 the nucleus and to quantify the number of cells with a “ring-like” TDP-43 staining appearance.
449 The nucleus, as defined by DAPI, was divided into three concentric regions using the Measure
450 Object Intensity Distribution module in CellProfiler and setting the number of bins to three. The
451 rings are therefore proportional to the size of each nucleus and nuclear area is accounted for in
452 the pipeline. For example, the outer ring represented the outer 1/3 of the nucleus, regardless of
453 nuclear size. TDP-43 fluorescent signal was measured within each of the three nuclear ring-
454 regions. Cells exhibiting ring-like TDP-43 staining were defined as those with >56% of the total
455 nuclear TDP-43 signal in the outer region (i.e., at the boundary of the nuclear envelope). This
456 threshold was determined by calculating the average percent of total nuclear TDP-43 signal
457 present in the outer region of the nucleus (the outermost concentric ring) in all WT sham cells
458 plus one standard deviation. Within a FOV, the percentage of cells with >56% nuclear TDP-43
459 signal in the outer nucleus out of the total cells per each condition was determined and used for
460 analysis.
461
462 The outcomes of the TDP-43 localization analyses above were combined to generate a measure
463 of cells with altered TDP-43 localization, which included cells that exhibited TDP-43 ring-like
464 and/or cytoplasmic TDP-43 according to the following parameters:
465

TDP-43 localization	N/C Ratio Value	% TDP-43 in outer ring of nucleus
Nuclear	>5.72	<56%
Ring-like, no cytoplasmic	>5.72	>56%
Ring-like with cytoplasmic	<5.72	>56%
Cytoplasmic, without ring-like	<5.72	<56%

466

467 The total number of cells that demonstrated each of the four TDP-43 distributions from the above
468 table (nuclear, ring-like +/- cytoplasmic and cytoplasmic) was summed then divided by the total
469 cells per FOV in each condition and multiplied by 100 to calculate the percent of cells with altered
470 TDP-43 localization per mouse. To visualize the overall effect of genotype and TBI on altered
471 TDP-43 localization, the percent of cells with each TDP-43 distribution was averaged across all
472 mice in each condition by FOV and plotted in a stacked bar graph in **Fig. 4**.

473

474 **Reverse transcription polymerase chain reaction (RT-PCR)**

475 RNA was isolated as described above and cDNA was synthesized using iScript Reverse
476 Transcription Supermix (Bio-Rad, 9170-8840) according to the manufacturer's instructions. RT-
477 PCR was performed on mouse tissue using 2x Taq RED Master Mix (APExBio Cat. No. K1034)
478 with the primers listed (**Supp. Table V**) with a touchdown PCR according to the manufacturer's
479 instructions. Products were separated on 3.5% agarose gels using the SYBR Safe DNA gel stain
480 (Invitrogen) and imaging was performed using the Bio-Rad Chemidoc software. Quantification of
481 the different isoforms was performed with ImageStudio software (LICORbio), using manual
482 settings to analyze the densitometry of each band. The intensity ratios between products with
483 included and excluded exons were analyzed for samples from a minimum of four individual mice
484 per group.

485

486

487 **Structural analysis**

488 The mm39 reference genome in Integrative Genomics Viewer, with its default RefSeq Curated
489 gene annotation track, was used to identify exons in *Ube3c*. The splice variant, with the
490 corresponding exon removed from the amino acid sequence, was modeled in AlphaFold 3.(66)
491 Structural alignments of the models were performed in PyMOL (Molecular Graphics System,
492 Version 3.1.3.1, Schrödinger) by minimizing the root-mean-square deviation (RMSD) between
493 superimposed structures. The resulting aligned structures were visualized in PyMOL.

494

495 **Ribosomal Profiling of cytoplasmic fractions**

496 Ribosomal profiling was performed as previously described (67) on cytoplasmic fractions. A 20%
497 to 50% sucrose gradient was prepared using a Gradient Master 107 (BioComp) in 14 x 89 mm
498 polypropylene ultracentrifuge tubes (Beckman 331372). A total of 6 mL of 20% sucrose solution
499 in 10 mM HEPES pH7.4, 150 mM NaCl, 5 mM MgCl2 with 100 μg/ml of cycloheximide, was added
500 and overlayed with 50% sucrose solution made using the same buffer conditions. The top of the
501 sucrose gradient (300 μl) was removed and replaced with 300 μl of sample (800 μg) containing
502 100 μg/ml of cycloheximide and 40 U/ml of RNaseIN. Samples were centrifuged at 197,000 x g
503 for 2h at 4°C using a Beckman SW41 Ti rotor. Samples were loaded on a Density Gradient
504 Fractionation system (Brandel), pushed with 60% sucrose and 0.72 ml fractions were collected
505 with real-time UV monitoring at 254 nm using an ISCO UA-6 UV detector. Protein was precipitated
506 from fractions using cold acetone. Protein pellets were collected by centrifugation at 13,000 x g
507 for 10 min at 4°C, resuspend in 100 μl of SDS loading buffer, and heated for 5 min at 90°C.

508

509 **RESULTS**

510 **Mutant TDP-43 mice exhibit heightened neurological deficits and delayed recovery**
511 **following TBI.** To examine the effects of TDP-43 dysfunction in the context of CNS challenge,

512 we administered a mild TBI using a weight-drop device (**Fig. 1A**) to mice harboring a knock-in
513 ALS-linked Q331K mutation in TDP-43.(44) TDP-43 Q331K mice (hereon referred to as Q331K
514 mice) exhibit phenotypes consistent with frontotemporal dementia (FTD), but without motor
515 deficits or motor neuron degeneration that is associated with ALS.(44) This mild TBI model has
516 been described by us previously.(39, 40, 43, 51, 52, 68) Here, a free-falling 50g weight was
517 dropped from a height of 15cm and used to deliver multiple impacts to the mouse's exposed but
518 intact skull within a single surgical session (**Fig. 1A,B**). Sham animals underwent the same
519 surgery as TBI animals to retract the skin from the skull but without any impact.

520 TBI studies included four main groups of mice at 16-weeks of age: Q331K and WT mice,
521 each with sham or TBI surgery. Neurological evaluations of motor function, alertness and
522 physiological behavior pre- and post-TBI were accomplished using a set of 10 tasks.(53) The
523 results of these tests are reported as a Neurological Severity Score (NSS), which is used to
524 assess potential neurological deficits following TBI in rodent models, where a higher score reflects
525 worse neurological deficits.(53). Consistent with our previous reports,(39, 43, 68) WT mice
526 exhibited worse NSS scores after TBI compared to their sham counterparts at 2 h post-TBI.
527 Notably, Q331K mice exhibited significantly worse NSS scores during the acute phase post-TBI
528 (i.e., 2h, 24h, and 48h post-TBI) compared to their WT counterparts, demonstrating heightened
529 vulnerability and delayed recovery to brain trauma **(Fig. 1C)**. All groups returned to baseline by
530 one-week post-TBI, as expected for a mild-TBI paradigm.(43)

531 Mice were also evaluated for long-term deficits resulting from TBI using the cued and contextual
532 fear conditioning (CCFC) test, an assessment of learning and memory.(69, 70) The CCFC test
533 consisted of four days, with habituation on day 1 (**Fig. 1D**), conditioning with a paired tone and
534 foot shock on day 2 (**Fig. 1E**), testing recall of the foot shock in response to the tone (i.e., cue) on
535 day 3 (**Fig. 1F**), and testing recall of the CCFC chamber (i.e., context) on day 4 (**Fig. 1G**). An
536 animal's freezing behavior on days 3 and 4 reflects its capacity for learning and memory, where

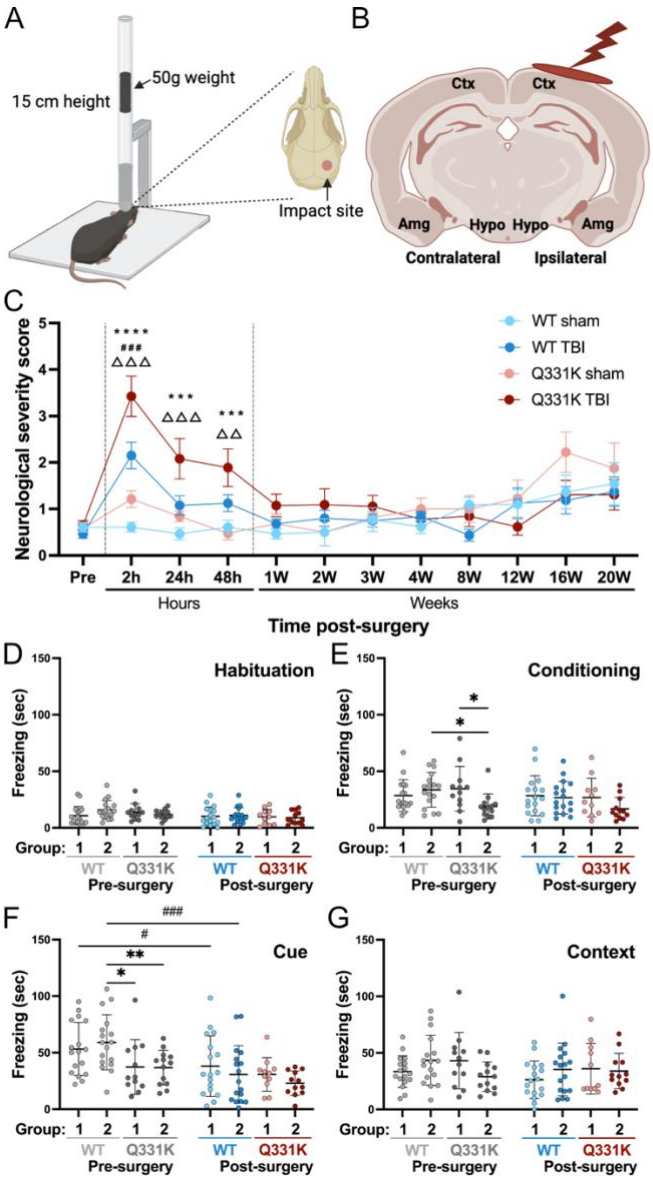

Figure 1. Neurological and cognitive deficits in mice with and without brain trauma. (A) Diagram of the weight drop device used to induce multiple closed-skull impacts with a 50g weight dropped from a 15cm height within a single surgical session. Location of impact site (red circle) is shown on the right. Created with biorender.com. **(B)** Illustration depicting the location of the impact site (red lightning bolt and oval). Several brain regions of interest are highlighted as follows: cortex (Ctx), amygdala (Amg), and hypothalamus (Hypo) on both ipsilateral and contralateral sides of the brain. Created with biorender.com. **(C)** Neurological severity score (NSS) plotted as a function of time post-surgery and cohort (see key). Statistically significant comparisons shown on the graph include Q331K TBI versus Q331K sham at 2h (****$p=2.98e^{-6}$), 24h (***p=0.00058) and 48h (***p=0.00018) post-surgery, WT TBI versus WT sham at 2h post-surgery ($^{\#\#\#}$p=0.00070) and Q331K TBI versus WT TBI at 2h ($^{\Delta\Delta\Delta}$p=0.00026), 24h ($^{\Delta\Delta\Delta}$p=0.00022) and 48h ($^{\Delta\Delta}$p=0.0058) post-surgery. Additional significant comparisons include Q331K TBI versus WT sham at 2h ($p=7.0e^{-10}$), 24h ($p=2.54e^{-6}$) and 48h (p=0.00014) post-surgery. **(D-G)** Mice were randomly assigned to Group 1 (sham) or 2 (TBI). Results of the cued and contextual fear conditioning (CCFC) test. **(E)** The Q331K-2 cohort exhibited altered freezing behavior during conditioning compared to Q331K-1 (*p=0.028) and WT-2 (*p=0.017). **(F)** Both Q331K cohorts exhibited attenuated cue-induced freezing relative to WT animals (*p=0.012 for WT-2 vs. Q331K-1; **p=0.009 for WT-2 vs. Q331K-2) pre-surgery. WT animals exhibited attenuated cue-induced 5-months after sham ($^{\#}$p=0.048) and TBI ($^{\#\#\#}$p<0.001) surgeries.

565 attenuated freezing is indicative of deficits in learning and memory.(69, 70) WT and Q331K mice
566 were randomly assigned to group 1 or group 2, and both groups were subjected to the CCFC test
567 before surgery. Group 1 and group 2 animals were then, respectively, administered sham or TBI
568 surgery and assessed using the CCFC test again 5-months post-surgery. Linear mixed effect
569 analyses were then used to determine potential differences between groups and over time (i.e.,
570 between pre- and post-surgery) for the CCFC test. This uncovered significant effects for the
571 conditioning (Day 2) and cue-induced freezing response (Day 3). For conditioning, significant
572 group (P=0.010; numerator degrees of freedom or df=3, denominator df=107.770, F=3.991)
573 effects were detected, but not significant time (P=0.139; df=1, denominator df=107.773, F=2.220)
574 or group x time interaction (P = 0.724; numerator df=3, denominator df=107.770, F=0.441) effects.
575 On pair-wise testing, one of the Q331K cohorts was found to exhibit altered freezing behavior
576 during conditioning compared to one of the WT cohorts and also to the other Q33K1 cohort (**Fig.**
577 **1E**). As mice were randomly assigned to groups 1 and 2, the reason for the latter difference in
578 pre-surgery mice is unclear. For cue-induced freezing response, significant group (P = 0.016;
579 numerator df=3, denominator df=107.938, F=3.595) and time (P <0.001; numerator df=1,
580 denominator df=107.955, F=14.651) effects were detected, but not significant group x time
581 interaction (P = 0.298; numerator df=3, denominator df=107.938, F=1.243) effects. On pair-wise
582 testing, both Q331K cohorts exhibited attenuated cue-induced freezing on day 3 relative to WT
583 animals, where comparisons with the WT-2 cohort reached significance (**Fig. 1F**). These
584 outcomes are consistent with Q331K mice exhibiting cognitive deficits prior to surgery, as shown
585 for other cognition tests described by White et al.(44)

586 Both WT sham and WT TBI groups showed differences in the cue-induced freezing response at
587 5 months post-surgery versus the pre-surgery timepoint (**Fig. 1F**). The reduced freezing behavior
588 in WT sham animals 5 months post-surgery may stem from aging and/or adverse effects related
589 to the sham surgery. Conversely, Q331K mice showed no difference in the cue-induced freezing

590 response at 5 months when compared to pre-surgery, when they already exhibited cognitive
591 deficits. Therefore, there may be a ceiling effect with respect to cognitive dysfunction in Q331K
592 mice, given that Q331K mice exhibit similar cue-induced freezing behavior pre- and post-surgery,
593 regardless of surgery-type or age (**Fig. 1F**). Finally, there were no significant differences in
594 context-induced fear behavior due to genotype or surgery (**Fig. 1G**). Taken together, this mild-
595 TBI paradigm appears to exert minimal long-term effects on learning and memory, whereas
596 mutant TDP-43 expression may be sufficient to cause deficits in the amygdala, the brain region
597 that influences cue-induced behavior more so than others such as the hippocampus.(69, 70)

598 **Proteostasis-related genes become upregulated in mutant TDP-43 mouse brain after TBI.**
599 To investigate the gene expression changes associated with enhanced neurological severity
600 scores and delayed recovery in Q331K mice (**Fig. 1C**), bulk RNA sequencing (RNAseq) was
601 pursued using mouse whole brain lysate near the impact site (**Fig. 1A**) at the 24h post-TBI
602 timepoint. This analysis focused on four groups: Q331K and WT mice, each with sham or TBI
603 surgery. Of the ~25,000 genes that remained after filtering out genes with very low expression,
604 our analysis identified 228 that were differentially expressed between the Q331K TBI and WT TBI
605 mice (**Fig. 2A, Supp. Table I**).

606 Gene Set Enrichment Analysis(59, 60) was performed using the hallmark and Gene Ontology
607 Biological Process (GOBP) gene set collections from the Molecular Signatures Database
608 (MSigDB).(56-58) The hallmark collection includes 50 gene sets, with clearly defined gene
609 expression, as a high-level representation of a compilation of other gene sets in MSigDB, whereas
610 GOBP represents >7000 gene sets capturing biological processes. A normalized enrichment
611 score (|NES|>1.5) and an adjusted p-value cutoff (FDR<0.05) were used to determine significantly
612 altered pathways between Q331K TBI and WT TBI mice. NES reflects the overrepresentation of
613 a gene set at the upper (positive value) or lower (negative value) end of a ranked gene list. GSEA
614 analysis of the hallmark collection identified “mammalian target of rapamycin complex 1

615 (MTORC1) signaling" as the top upregulated gene set (**Fig. 2B**; **Supp. Table II**). MTORC1
616 signaling is involved with multiple cellular processes, including protein synthesis and
617 autophagy.(71) Protein folding was associated with the top 3 gene sets from GOBP identified in
618 the GSEA analysis (**Fig. 2C**). The relative expression for the top 30 ranked genes in the "MTORC1
619 signaling" (**Fig. 2D**) and "protein folding" (**Fig. 2E**) pathways are shown in a heatmap
620 representation, highlighting striking differences in gene expression between Q331K TBI mice
621 relative to the other three cohorts. Seven genes overlap between the top ranked list for MTORC1
622 signaling and protein folding, with *Hspa5*, encoding the endoplasmic reticulum (ER)-associated
623 chaperone heat shock 70 kDa protein 5, as the top ranked gene in both pathways (**Fig. 2D-E**).

624 To further examine differentially expressed genes between Q331K and WT mice as a function of
625 TBI, we compared significant transcriptional changes in Q331K TBI versus Q331K sham mouse
626 brain lysates (**Fig. S2A and Supp. Table I**) with those in WT TBI versus WT sham (**Fig. S2B and**
627 **Supp. Table I)** by plotting directional p-values (**Fig. 3A**), in which $-\log_{10}$(p-value) – a measure of
628 significance – is multiplied by the sign of the $\log_2$(fold-change), so that negative scores reflect a
629 decrease in gene expression for a specific comparison and positive scores reflect an increase in
630 expression. In this plot, genes that significantly change in expression in the Q331K TBI versus
631 Q331K sham comparison (sections shaded in pink) can be visualized along the x-axis, whereas
632 the y-axis highlights genes that significantly change in expression in WT TBI versus WT sham
633 mice (sections shaded in blue). Sections shaded in grey highlight genes that are differentially
634 expressed as a function of TBI, irrespective of genotype (**Fig. 3A**), and include 63 genes with
635 FDR<0.1 in both comparisons (**Fig. 3B, Supp. Table I**). GSEA hallmark pathway analysis
636 revealed "TNFa signaling via NFkB" as the top ranked, upregulated pathway in both Q331K (**Fig.**
637 **3C and Fig. S2C**) and WT (**Fig. 3D and Fig. S2D**) brain lysates post-TBI relative to their sham
638 counterparts (**Supp Table II**). This is not surprising, given that inflammation and changes in innate
639 immunity-related processes are well-documented following brain trauma.(72) Pathway changes

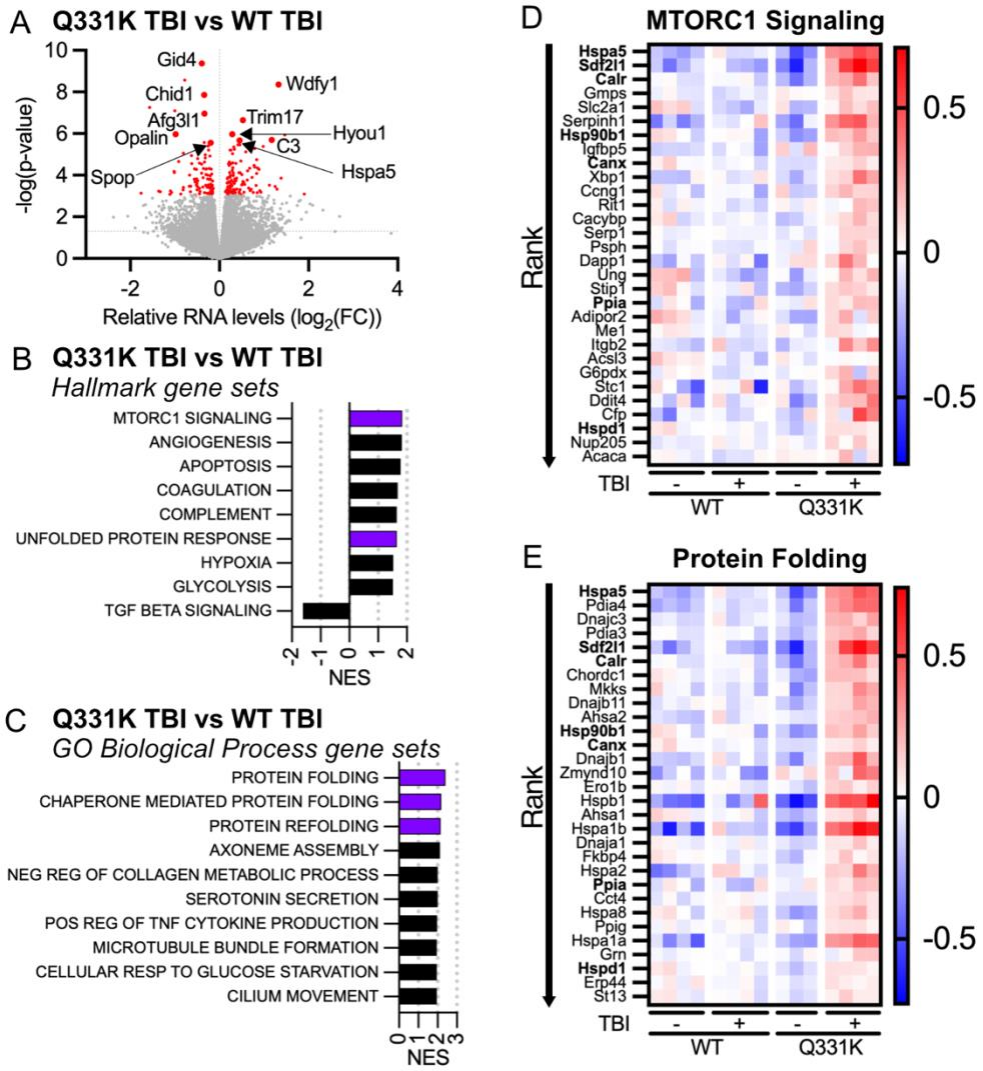

Figure 2. Upregulation of MTORC1 and protein folding genes in Q331K versus WT mouse brain after TBI. (A) Volcano plot of RNAseq data comparing Q331K and WT mice, each with either TBI or sham surgery. Differentially expressed genes (DEGs) with FDR <0.1 are shown in red. Top up- and down-regulated annotated genes are labeled. **(B,C)** Top GSEA gene set hits (both up and down regulated, as applicable) for Q331K TBI relative to WT TBI using the Molecular Signatures Database (MSigDB) hallmark **(B)** and Gene Ontology Biological Process **(C)** collections. Purple bars denote gene sets associated with proteostasis. **(D,E)** Heatmaps showing the top 30 ranked genes in the hallmark gene set "MTORC1 signaling" **(D)** and the Gene Ontology Biological Process gene set "protein folding" **(E)**. The $\log_2$(fold change) relative to the mean expression is shown for each sample. All pathway hits meet cutoff criteria of

650 FDR <0.05 and |NES|>1.5. Genes in both “MTORC1 signaling” and “protein folding” gene sets are indicated
651 in bold.
652
653
654
655
656
657
658
659
660
661
662
663
664
665
666
667
668
669

670 that were specific to the WT TBI versus WT sham comparison indicate a downregulation of
671 metabolic and bioenergetic processes that occur in the mitochondria, such as “oxidative
672 phosphorylation” and “NADH dehydrogenase complex assembly” (**Fig. 3D,E and Fig. S2E,F**).
673 TBI is known to affect mitochondrial bioenergetics, where TBI induces mitochondrial damage and
674 results in reduced energy production.(73) Although these pathways were not significantly altered
675 between Q331K TBI and Q331K sham brain lysates, expression of genes in these pathways were
676 variable and potentially dysregulated in Q331K mice under both TBI and sham conditions, an
677 observation that may reflect transient and adverse effects of mutant TDP-43 on mitochondria
678 reported by others.(74)

679 Strikingly, nine out of the top ten GOBP gene sets emerging from the Q331K TBI versus Q331K
680 sham comparison were proteostasis-related, including protein folding and response to ER-stress
681 (**Fig. 3F**), which were not enriched gene sets in the WT TBI versus WT sham comparison (**Fig.**
682 **3D, Supp Table II**). Further, proteostasis-related genes *Hspa5*, mesencephalic astrocyte-derived
683 neurotrophic factor (*Manf*), calreticulin (*Calr*) and protein disulfide isomerase family A, members
684 3 (*Pdia3*) and 6 (*Pdia6*) were significantly increased in Q331K TBI versus Q331K sham mice (**Fig.**
685 **3A**; pink-shaded region). Proteostasis-related gene expression changes did not persist long-term
686 post-TBI, as determined by a separate RNA-seq analysis on whole brain mouse lysates 7-months
687 post-TBI or sham surgery, for both WT and Q331K mice. In fact, there were no significant gene
688 expression changes (at cutoff FDR < 0.1) due to TBI for either genotype (i.e., Q331K TBI versus
689 Q331K sham and WT TBI versus WT sham; **Supp Table I**).

690 Considering the upregulation of transcripts involved in protein folding and ER-stress in Q331K
691 mice 24h post-TBI compared to the other three cohorts, we assessed protein level changes with
692 quantitative proteomics analysis of mouse brain lysates labeled with tandem mass tags (TMTs)
693 from the four cohorts. Other than TDP-43, no significantly upregulated proteins were detected
694 (**Fig. S3A, Supp Table III**). In fact, TDP-43 upregulation was observed in Q331K versus WT

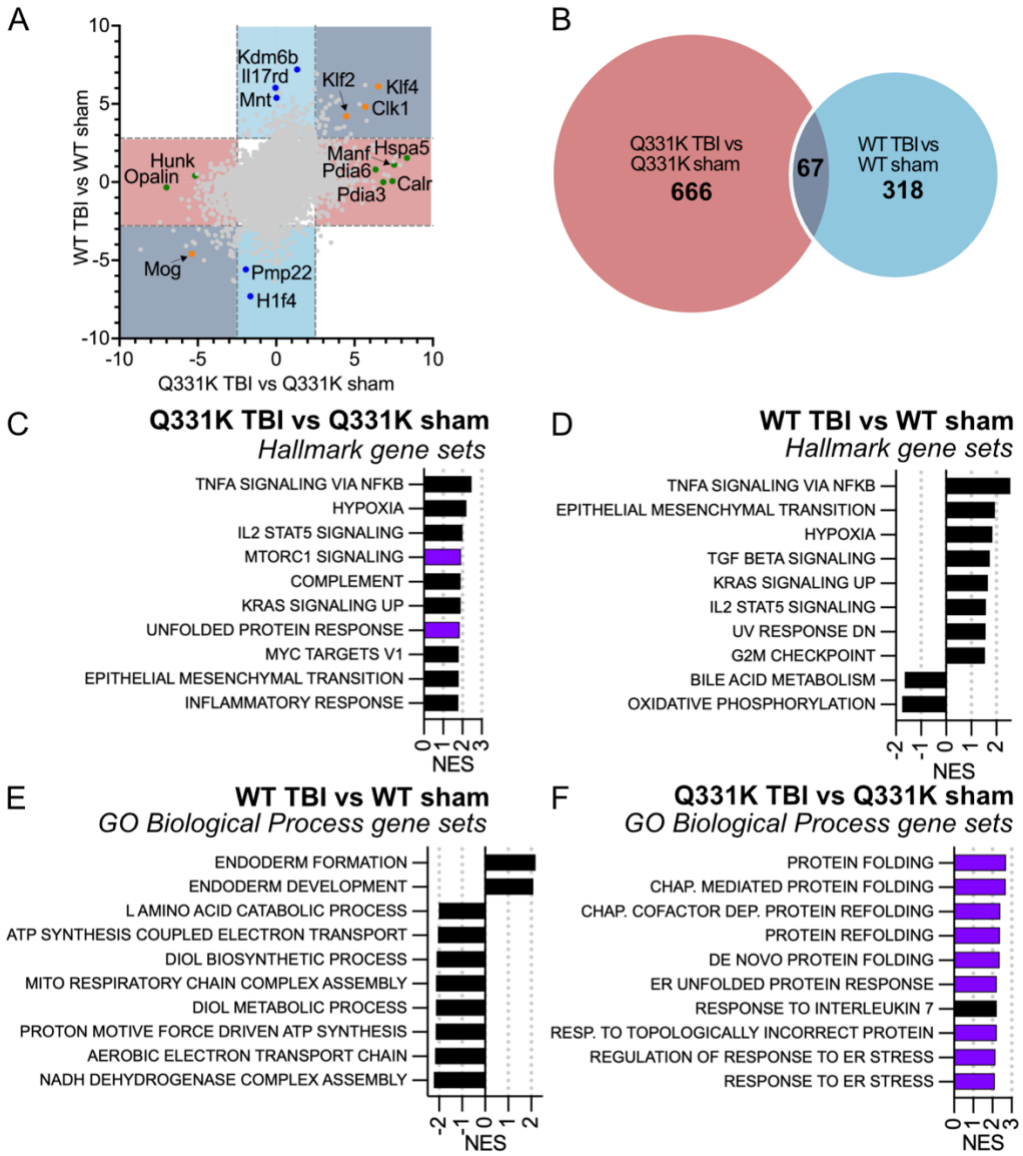

Figure 3. Differentially expressed genes in WT and Q331K mouse brain as function of surgery. (A) Plot of directional p-values (-$\log_{10}$(p-value)*sign of $\log_2$(fold change)) from transcriptomics datasets for the WT TBI versus WT sham comparison plotted against the Q331K TBI versus Q331K sham comparison. The sign of the score reflects the direction of the fold change. Orange dots denote genes with expression changes specifically due to TBI, irrespective of genotype. Blue and green dots denote genes with expression changes specifically in WT and Q331K mice, respectively, after TBI. Color-shaded sections indicate unique and overlapping gene changes, as illustrated in B. Dotted lines indicate FDR=0.1 **(B)** Venn diagram illustrating minimal gene overlap between Q331K and WT mice subjected to TBI using FDR <0.1. **(C-F)** Top GSEA gene set hits from the RNAseq analysis for Q331K TBI versus Q331K sham conditions

705 using the hallmark collection **(C)**, WT TBI versus WT sham conditions using the hallmark collection **(D)**, WT
706 TBI versus WT sham conditions using the Gene Ontology Biological Process collection **(E)** and Q331K TBI
707 versus Q331K sham conditions using the Gene Ontology Biological Process collection **(F)**. All gene set hits
708 meet cutoff criteria of FDR <0.05 and |NES|>1.5. Purple bars denote gene sets that are associated with
709 proteostasis.
710
711
712
713
714
715
716
717
718
719
720
721
722
723
724
725
726

727 comparisons irrespective of surgery type, at both mRNA and protein levels (**Fig. S3C,D**),
728 consistent with a loss of TDP-43 autoregulation due to the Q331K mutation.(44) Despite a
729 significant upregulation of *Hspa5* at the mRNA level in Q331K TBI mice, differential expression of
730 Hspa5 protein was not observed across the four mouse cohorts (**Fig. S3B)**. We additionally
731 probed for isoforms of active X-box binding protein 1 (Xbp1; **Fig. 2D**), which becomes spliced
732 (Xbp1s) and activated under conditions of ER-stress (**Fig. 3F**),(75) by Western blot analysis.
733 Xbp1s was not detected in samples from any mouse cohort and levels of unspliced Xbp1 (Xbp1u)
734 were unchanged across conditions (**Fig. S3E**). The apparent lack of upregulation at the protein
735 level may be due to deficits in protein synthesis or because 24h post-TBI is too early a timepoint
736 for detection of newly translated protein. Nonetheless, the transcriptomics data clearly indicate a
737 robust upregulation of proteostasis-related pathways at the mRNA level that is dependent on both
738 TBI and expression of mutant TDP-43.

739 To gain insight into the relevance of our TBI model to neurodegenerative diseases such as ALS
740 and FTLD-TDP, we compared the GSEA hallmark gene set analyses of the TBI versus sham
741 conditions for both WT and Q331K mice with recent transcriptomic analyses of human ALS post-
742 mortem spinal cord and FTLD-TDP brain tissues.(45, 46) Significantly upregulated gene sets in
743 FTLD-TDP and/or ALS CNS tissues, such as “TNFa signaling via NFkB” and “hypoxia”, were also
744 significantly upregulated in our TBI model, irrespective of genotype (**Fig. S4**). Notably, several
745 significantly upregulated gene sets in FTLD-TDP and/or ALS CNS post-mortem tissues were only
746 observed in Q331K mice after TBI, but not WT mice after TBI, including “MTORC1 signaling”,
747 “unfolded protein response” and “inflammatory response” (**Fig. S4**). Similarly, GO terms related
748 to cytoplasmic translation and innate immunity emerged from a single nucleus sequencing
749 analysis of neurons from a separate study of human post-mortem ALS and FTLD brain tissue.(76)
750 Therefore, there appears to be a synergistic effect of mutant TDP-43 dysfunction and acute brain

751 trauma on biological processes in the CNS that, at least partially, recapitulates neurodegenerative
752 disease processes on the ALS/FTLD spectrum.

753 **Proteostasis-related factors and pathways are downregulated in mutant TDP-43 mice at**
754 **baseline.** We performed similar omics analyses on cohorts of WT and Q331K mice without TBI,
755 including RNAseq on mice without surgery (i.e., naïve mice). In our view, the sham condition
756 represents the most relevant control for TBI, as it accounts for gene expression changes that
757 occur from the surgery itself, thereby revealing expression changes due to the impact. Including
758 naïve mice here serves as an additional control for identifying differentially expressed genes due
759 to expression of mutant TDP-43. For the Q331K versus WT sham comparison, only two
760 downregulated gene sets emerged from our GSEA analysis, "protein folding" and "aerobic
761 electron transport chain" (**Supp. Table II**). Similarly, "MTORC1 signaling", which includes
762 proteostasis-related genes, such as heat shock protein family chaperones *Hspd1*, *Hspe1*, and
763 *Hspa4*, was a downregulated pathway for the Q331K versus WT naïve comparison (**Supp. Table**
764 **II**). Plotting transcriptomics data with directional p-values for the Q331K versus WT sham groups
765 against Q331K versus WT naïve groups revealed a significant downregulation of genes involved
766 in the ubiquitin-proteosome pathway, including glucose-induced degradation protein 4 homolog
767 (*Gid4*) and speckle-type POZ protein (*Spop*), the latter a downregulated gene that was also
768 observed by White et al. in this Q331K model (**Fig. S5B** and **Supp. Table IV**).(44) Of note, both
769 *Gid4* and *Spop* remain downregulated in Q331K sham and TBI mice at 7 months post-TBI relative
770 to WT groups (**Supp. Table I, Fig. S5C,D**). Further, our quantitative proteomics analysis of Q331K
771 versus WT sham groups uncovered a modest yet significant decrease in the large ribosomal
772 subunit protein P1 (Rplp1), which plays a critical role in embryonic and brain development (**Fig.**
773 **S3F**, **Supp. Table III**).(77) Collectively, these omics data point toward a deficit in proteostasis-
774 related pathways in Q331K mice at baseline.

775 **TDP-43 exhibits altered nuclear and cytoplasmic localization following TBI.** Different TBI
776 models reportedly induce subcellular redistribution of TDP-43 from the nucleus, where the protein
777 is predominately expressed under homeostatic conditions, to the cytoplasm.(13, 37-41)
778 Enhanced cytoplasmic localization of TDP-43 is also well-documented in other stress paradigms
779 in vivo and in vitro, indicating that subcellular redistribution of TDP-43 represents a physiological
780 response to stress.(2-6, 78) Given the disparate responses between Q331K and WT mice to TBI
781 (**Figs. 1-3**), we examined the cellular localization of TDP-43 in situ as a function of surgery and
782 TDP-43 genotype. Mouse brain tissue sections from TBI and sham cohorts were stained with anti-
783 TDP-43 antibody and counterstained with DAPI. Obvious changes in subcellular TDP-43
784 distribution were observed in the cortex, amygdala, and hypothalamus (regions defined in **Fig.**
785 **1B**) of both Q331K and WT mice (**Fig. 4**), whereas changes in TDP-43 subcellular distribution
786 were minimal or not detected in other regions of the tissue section (not shown). Sham animals
787 also exhibited some degree of cytoplasmic TDP-43 redistribution in these brain regions, possibly
788 indicative of cellular "stress" caused by the sham surgery, and therefore the naïve condition was
789 included here for further analysis.

790 To quantify TDP-43 cellular localization, confocal microscopy images were acquired within the
791 cortex, amygdala, and hypothalamus of Q331K and WT mice in the absence of surgery (i.e.,
792 naïve) or 24h after receiving a sham or TBI surgery, for a total of six groups (**Fig. 4A,B**). First,
793 TDP-43 nuclear-to-cytoplasmic (N/C) ratios were determined for all cells across a field of view
794 (FOV) on a per image basis. Reductions in TDP-43 N/C in TBI versus naïve conditions were
795 generally observed in all three brain regions for both WT and Q331K mice, although some
796 comparisons did not reach statistical significance (**Fig. S6A**). Notably, TBI-induced reductions in
797 TDP-43 N/C ratios occurred in both ipsilateral (i.e., TBI side) and contralateral hemispheres of
798 the brain (**Fig. S6A**) and were prominent in the amygdala and hypothalamus. Therefore, the
799 effects of TBI on subcellular TDP-43 localization extend beyond the site of injury in the cortex,

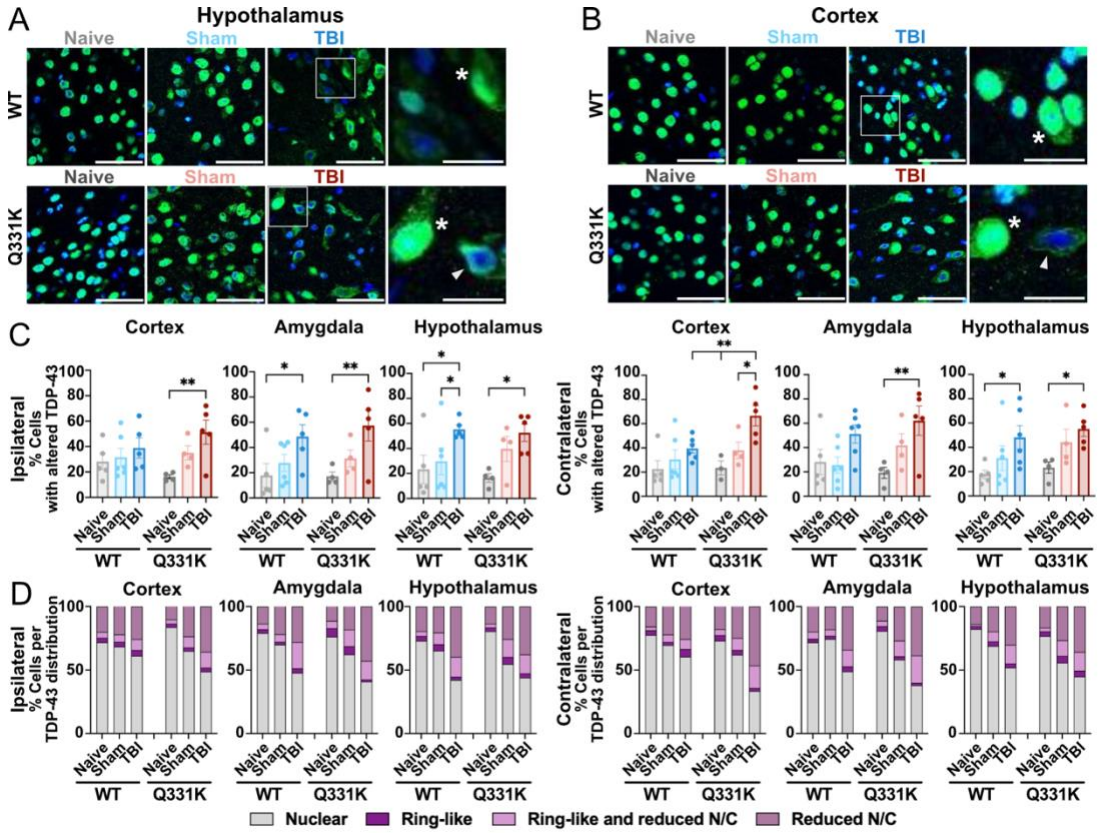

Figure 4. Alterations in TDP-43 localization in WT and Q331K mice as a function of surgery. (A-B) Confocal immunofluorescence images from WT and Q331K mice under native (i.e., no surgery) conditions or 24h post-surgery (sham and TBI). Tissues were stained for TDP-43 (green) and counterstained with DAPI (blue). Images from the hypothalamus (A) and cortex (B) are shown. Cropped insets highlight cells with cytoplasmic (asterisks) and ring-like distribution (triangles) of TDP-43 under conditions of TBI. Scale bar=50 um in the low magnification image and =20 um in the insets. **(C)** Percent of cells that exhibit altered TDP-43 localization (ring-like, reduced nuclear-to-cytoplasmic (N/C) ratio, or both) in the cortex, amygdala, or hypothalamus, either ipsilateral (left) or contralateral (right) to the impact site 24h post-surgery. (**D)** Stacked bar graphs representing the average percent of cells that exhibit nuclear TDP-43 localization (grey) or a type of altered TDP-43 localization (defined in C and color-coded according to the key) within the indicated brain region. **(C-D)** Quantification of TDP-43 localization was performed using tissues from n=4-6 mice, where each dot represents a different mouse. Statistical analysis was performed using two-way ANOVA followed by Tukey's multiple comparisons test: *p<0.05, **p<0.01, ***p<0.001, ****p<0.0001.

814 likely because the weight-drop induces contact between the skull and brain tissue at the base of
815 the skull (**Fig. 1A,B**). TBI-induced changes in TDP-43 subcellular localization represented an
816 acute response to TBI, as differences in TDP-43 N/C ratios were no longer observed at 5-months
817 post-surgery (**Fig. S7**).

818 As changes in TDP-43 subcellular localization were not observed in every cell, the percentage of
819 cells exhibiting reduced TDP-43 N/C ratio relative to the naïve condition was determined from the
820 FOVs above. Q331K TBI mice exhibited a significantly higher percentage of cells with reduced
821 TDP-43 N/C ratio in all three brain regions relative to Q331K naïve mice for both ipsilateral and
822 contralateral hemispheres, which was collectively a more robust change than for their WT
823 counterparts (**Fig. S6B**). During this analysis, we also noticed a "ring-like" TDP-43 staining
824 pattern, which appeared as dense TDP-43 signal near the outer edge of (but still within) the
825 nucleus (**Fig. 4A**, Q331K inset) and that also occurred in cells with cytoplasmic TDP-43 staining.
826 We developed a CellProfiler pipeline (see Methods) to quantify the percentage of cells with this
827 phenotype and found significant ring-like TDP-43 staining in TBI versus control comparisons in
828 all brain regions for at least one genotype (**Fig. S6C**). Ring-like TDP-43 staining was most
829 prominent in the hypothalamus and amygdala for both Q331K TBI and WT TBI mice versus their
830 respective controls, on both sides of the brain (**Fig. S6C**).

831 To assess the full extent of altered TDP-43 subcellular localization after TBI, we compiled the
832 data above (**Fig. S6**) and determined the percentage of cells exhibiting reduced TDP-43 N/C ratio
833 and/or ring-like TDP-43 (**Fig. 4C,D**). TBI induced more pronounced changes in TDP-43
834 localization in the cortical region below the impact site in Q331K versus WT mouse brain,
835 particularly on the contralateral side (**Fig. 4C,D**). These analyses also highlighted that Q331K
836 sham animals exhibited significant TDP-43 subcellular localization changes that were more
837 similar to the Q331K TBI condition and were significantly different than their Q331K naïve
838 counterparts, especially in the hypothalamus (**Fig. S6B,C**). Taken together, these data

839 demonstrate an acute response involving the TDP-43 protein to brain injury that occurred
840 irrespective of genotype. That Q331K mice appeared to be more sensitive to both sham and TBI
841 surgery with respect to changes in subcellular TDP-43 localization further supports the notion that
842 TDP-43 dysfunction leads to altered stress responses in vivo.

843 **Effects of TDP-43 mutation and TBI on select TDP-43 splice targets.** An important nuclear
844 function of TDP-43 involves the alternative splicing of conserved exons for numerous RNA
845 targets,(1) which can become mis-spliced as a result of TDP-43 knock-down, overexpression
846 and/or mutation.(79, 80) We therefore considered whether TBI-induced subcellular redistribution
847 of TDP-43 (**Fig. 4** and **Fig. S6**) would manifest in altered splicing of TDP-43 RNA targets. To
848 address this possibility, we probed for potential changes in splicing patterns for eight known RNA
849 targets of TDP-43 within mouse brain lysates derived from near the TBI site (**Fig. 1A**) using RT-
850 PCR and primer sequences that cover the exon junctions of interest (**Supp. Table V**). TDP-43
851 RNA targets included several that become mis-spliced due to TDP-43 misexpression, including
852 DnaJ heat shock protein family (Hsp40) member 5 (*Dnajc5*), potassium voltage-gated channel
853 interacting protein 2 (*Kcnip2*), protein phosphatase 3 catalytic subunit alpha (*Ppp3ca*), and
854 translin (*Tsn*).(81-84) Splicing patterns were assessed by gel electrophoresis (**Fig. 5A**) and
855 reported as the fraction of the mis-spliced variant versus the common or more abundant variant
856 expressed under normal conditions (**Fig. 5B**). For *Dnajc5*, no differences in splicing of exon 5
857 were observed between the mouse groups studied herein. In contrast, enhanced exon exclusion
858 most consistent with TDP-43 loss-of-function was detected for Q331K mice, irrespective of
859 surgery, for *Kcnip2* (exon 3 only, indicated by an increase in S1), *Ppp3ca* and *Tsn*.(84) Consistent
860 with TDP-43 gain-of-function reported in this and other Q331K mouse models,(44, 82) enhanced
861 exclusion of exon 17b in Sortilin-1 (*Sort1*) was observed in both Q331K TBI and sham mice; in
862 contrast, inclusion of exon 17b correlates with TDP-43 loss-of-function.(29, 81-83)
863

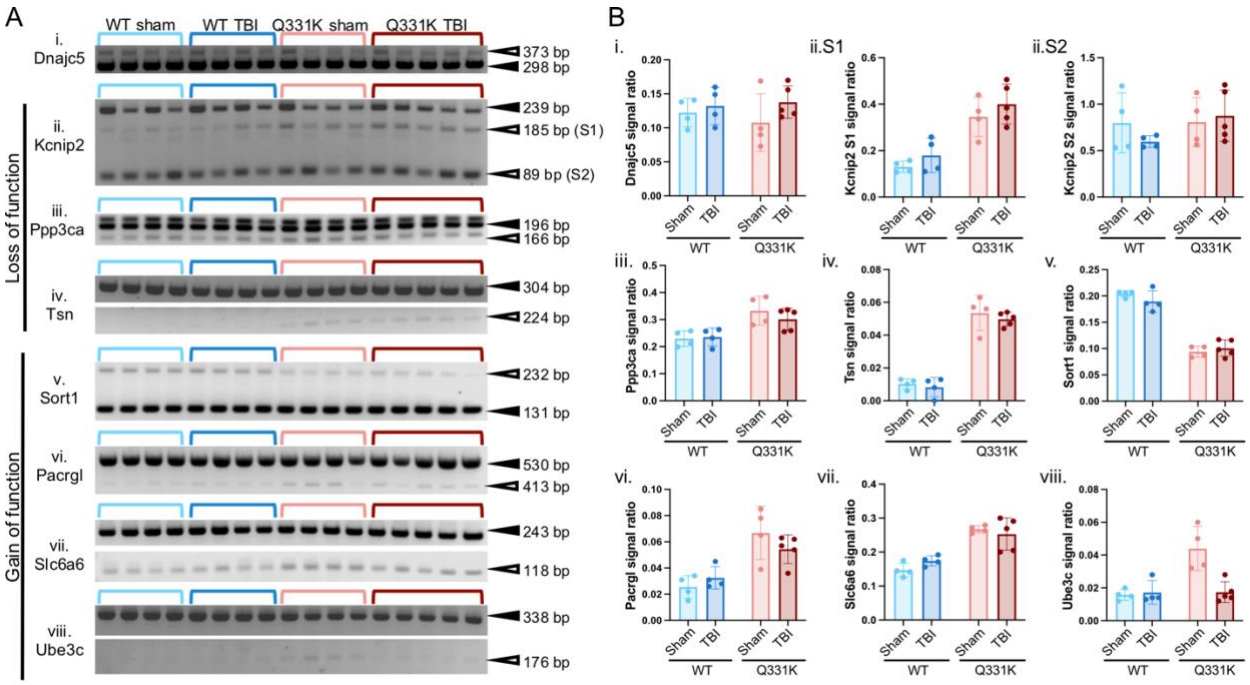

Figure 5. **Alternative splicing patterns for TDP-43 targets in WT and Q331K mouse brain after TBI.** **(A)** Splice variants of known TDP-43 RNA targets (i-vi) detected by RT-PCR analysis in WT and Q331K mice 24h after either TBI or sham surgery. The PCR primers, exons of interest and references for the primers used in this study are shown in **Supp Table VI**. Splicing patterns that are consistent with TDP-43 loss of function or gain of function are indicated. Common and mis-spliced variants are denoted by, respectively, closed and open arrowheads with the corresponding size (bp=base pairs) of the PCR product. Gels are representative of at least n=3 separate RT-PCR experiments. **(B)** Densitometry analysis of the gels in (A) was used to determine the ratio of the mis-spliced/common PCR product for each gene of interest. Each dot in the graph represents a separate mouse.

881 We examined additional genes with known skiptic exons caused by mutant TDP-43 gain-of-
882 function in vivo.(80, 82) These included parkin coregulated like (*Pacrgl*), solute carrier family 6
883 member 6 (*Slc6a6*) and ubiquitin protein ligase E3C (*Ube3c*).(82) Skiptic exons were detected in
884 Q331K samples for all three genes. Intriguingly, the skiptic exon in *Ube3c* was attenuated in
885 Q331K mice after TBI, thus representing a gene-splicing event that was modulated by TBI,
886 specifically in Q331K mice (**Fig. 5A,B**). *Ube3c* encodes an E3 ubiquitin ligase that promotes
887 proteasomal degradation of misfolded proteins.(85) TDP-43-mediated skipping of exon 6 in
888 *Ube3c* causes the removal of 54 amino acid residues between the ubiquitin-binding domain and
889 the catalytic Homologous to the E6-AP Carboxyl Terminus (HECT) domain (**Fig. S8A**). While the
890 impact of exon 6 removal on Ube3c function is unknown,(82) modeling the 3-dimensional protein
891 structure of Ube3c in AlphaFold(66) suggests that omission of exon 6 could induce conformational
892 perturbations in the protein N-terminal to the HECT domain (**Fig. S8B**). The effects of TBI on
893 *Ube3c* exon 6 skipping in Q331K mice were acute, as exon skipping was no longer observed at
894 7-months post-TBI. Additionally, the splicing patterns for the other seven candidate TDP-43
895 mRNA targets were unchanged at 7-months post-TBI compared to 24h post-TBI (**Fig. S9**). Taken
896 together, these RT-PCR results indicate that TBI-induced changes in subcellular TDP-43
897 localization do not strongly correlate with a loss of TDP-43 splicing function, as most of the
898 observed splicing differences were due to TDP-43 mutation and not TBI. An exception is TDP-43
899 Q331K-induced skipping of exon 6 in *Ube3c*, which is attenuated during the acute phase post-
900 TBI.

901 **Ribosomal proteins exhibit thermal instability in Q331K mice.** A cytoplasmic shift in TDP-43
902 localization appears to represent a physiological response to brain trauma in mice, irrespective of
903 TDP-43 genotype (**Fig. 4**). We hypothesized that mutations in TDP-43 could alter the nature of
904 this response by perturbing cytoplasmic cellular processes involved in stress recovery. For
905 example, disease-linked mutations in TDP-43 have been shown to affect the interaction of TDP-
906 43 with cytoplasmic RNA granules as well as the biophysical properties of these granules.(11, 12,

907 14-16) Here, we examined protein content and protein thermostability of mouse brain lysates in
908 both WT and Q331K mice after sham or TBI surgery using the Proteome Integral Solubility
909 Alteration (PISA) assay (**Fig. S10A**) coupled with TMT quantitative proteomics using mass
910 spectrometry.(86, 87) PISA capitalizes on the principle that proteins become insoluble when
911 denatured. By extension, how a protein partitions between the soluble and insoluble fraction as a
912 function of temperature can be used to detect changes in protein thermostability under various
913 conditions. PISA and similar assays were historically used to elucidate protein targets of small
914 molecules, which generally induce an increase in thermostability of their protein targets upon
915 binding.(86, 88) We reasoned that PISA could be repurposed here for identifying thermostability
916 shifts of cytosolic proteins and protein complexes in brain lysates as a function of TBI and TDP-
917 43 mutation. To simplify sample processing and analysis, lysates were first depleted of large
918 organelles. A Western blot analysis with histone H3 and cytochrome c oxidase subunit IV (CoxIV)
919 antibodies confirmed that this protocol depleted nuclei and mitochondria, respectively, whereas
920 anti-calreticulin confirmed that ER was retained (**Fig. S10B**).

921 For the PISA assay, lysates were subjected to a narrow temperature gradient (52-54°C) followed
922 by centrifugation to remove the insoluble protein (**Fig. S10A**). The resulting soluble fraction was
923 subjected to quantitative proteomics (**Fig. S10C**). In parallel, quantitative proteomics was
924 performed on cytosolic lysates without heat exposure to determine total protein levels (**Fig.**
925 **S10D**). Only modest differences in total protein levels between Q331K TBI and WT TBI cytosolic
926 lysates were detected by the proteomic analysis (**Fig. S10D and Supp. Table VI)**, for which no
927 gene sets were significantly enriched by GSEA (**Supp. Table VII**). In striking contrast, GSEA
928 analysis of the PISA proteomics for the Q331K TBI versus WT TBI comparison revealed multiple
929 downregulated processes, with seven of the top ten GOBP hits including terms for translation and
930 ribosome (**Fig. 6A**). As shown in the heatmap for “cytoplasmic translation” (**Fig. 6B**), ribosomal
931 proteins account for most of the top 30 proteins in this pathway. Proteins in the “cytoplasmic

932 translation" pathway become elevated within the soluble fraction from WT animals after TBI
933 compared to their sham counterparts, as demonstrated in the heatmap (**Fig. 6B**) and a box plot
934 for the top five ranked proteins in the heatmap, all of which are ribosomal proteins (**Fig. 6C**).
935 Conversely, these ribosomal proteins are diminished within the soluble fraction from Q331K sham
936 mice relative to WT mice, and while they do become enhanced after TBI, their levels remain
937 significantly below that of WT TBI lysates (**Fig. 6B,C**).

938 Considering that decreased protein solubility in the PISA assay is indicative of reduced protein
939 thermostability, our interpretation of the PISA outcomes is that ribosomal proteins and potentially
940 ribosome complexes themselves exhibit reduced thermostability in Q331K mice relative to WT
941 mice. Polysome profiling of cytosolic lysates confirmed that intact 80S ribosomes were indeed
942 present for both WT and Q331K conditions (**Fig. S11A-C**). RNA fragment analysis of isolated
943 RNA confirmed the presence of both 28S and 18S ribosomal RNA (**Fig. S11D**). Given that the
944 effect of TDP-43 Q331K expression on ribosome stability occurred irrespective of surgery, and
945 that moreover there were no proteins for which the genotype x injury interaction contrast was
946 significant (FDR < 0.1) in the limma linear model, we focused on the main effect of genotype for
947 additional proteomic analyses. This approach further verified that total levels of ribosomes in the
948 cytosolic lysates were unchanged between TDP-43 genotypes (**Fig. 6D**), but that their
949 thermostability was reduced in Q331K mice relative to WT mice (**Fig. 6E**). We note that Rplp1,
950 which was reduced in the proteomics analysis of total brain lysates (**Fig. S3F**), was not
951 quantifiable in the cytosolic proteomics because only one unique peptide was identified whereas
952 ≥2 were required in our pipeline for protein level quantification (**Supp. Table VI**). A subsequent
953 STRING analysis using Markov Clustering (MCL) for the 50 destabilized proteins (FDR < 0.1)
954 revealed a major cluster of 27 proteins (Cluster 1) associated with "cytoplasmic translation" and
955 "ribosome" (**Fig. 6F**).(89, 90) Importantly, most of the ribosomal proteins in this cluster were
956 shown to immunoprecipitate with TDP-43 from cultured cell and/or mouse brain lysates, raising

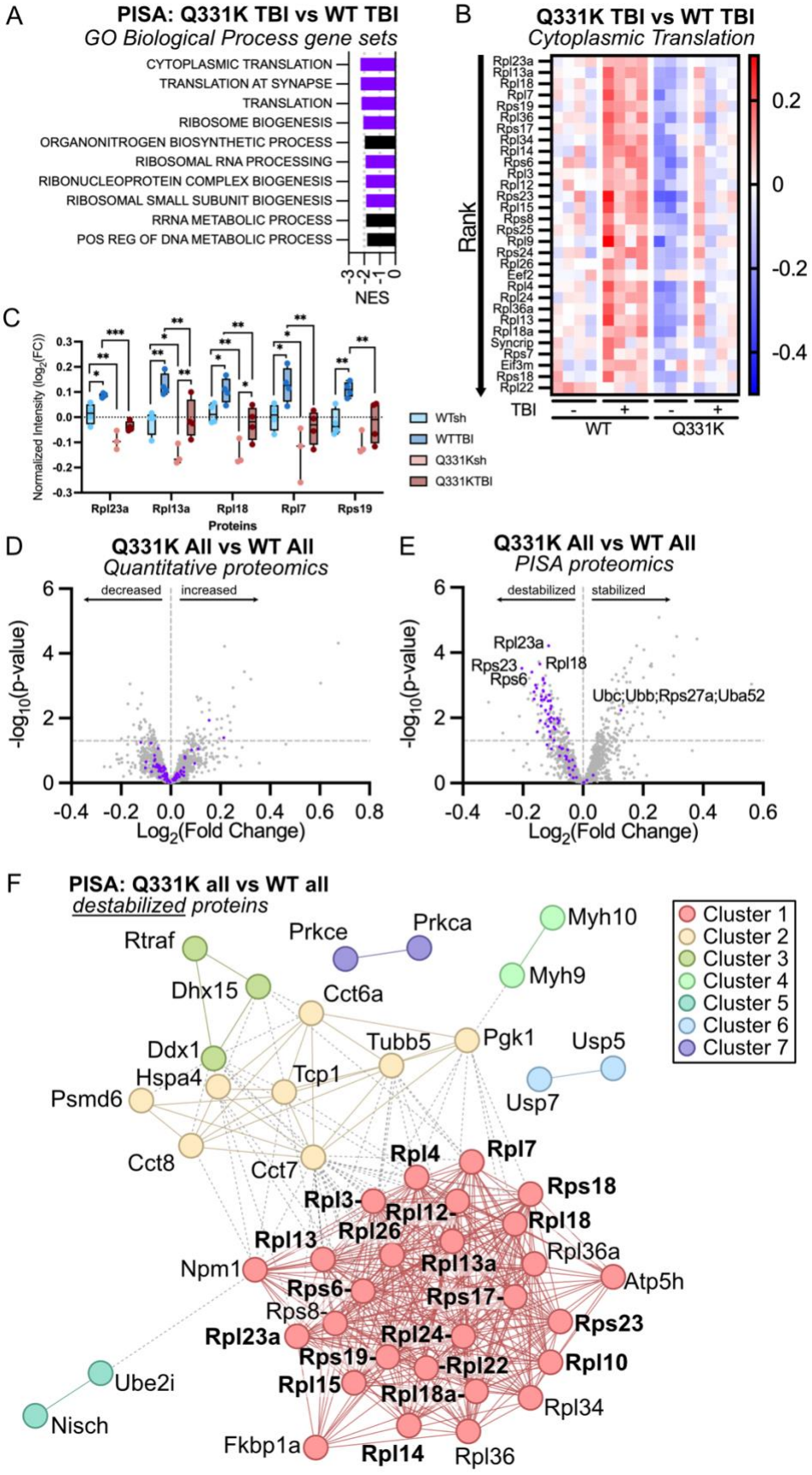
A
PISA: Q331K TBI vs WT TBI
GO Biological Process gene sets
CYTOPLASMIC TRANSLATION
TRANSLATION AT SYNAPSE
TRANSLATION
RIBOSOME BIOGENESIS
ORGANONITROGEN BIOSYNTHETIC PROCESS
RIBOSOMAL RNA PROCESSING
RIBONUCLEOPROTEIN COMPLEX BIOGENESIS
RIBOSOMAL SMALL SUBUNIT BIOGENESIS
RRNA METABOLIC PROCESS
POS REG OF DNA METABOLIC PROCESS
NES
B
Q331K TBI vs WT TBI
Cytoplasmic Translation
Rank
TBI
WT
Q331K
C
Normalized Intensity (log2(FC))
Rpl23a
Rpl13a
Rpl18
Rpl7
Rps19
Proteins
WTsh
WTTBI
Q331Ksh
Q331KTBI
D
Q331K All vs WT All
Quantitative proteomics
decreased
increased
-log10(p-value)
Log2(Fold Change)
E
Q331K All vs WT All
PISA proteomics
destabilized
stabilized
Rpl23a
Rps23
Rpl18
Rps6
Ubc;Ubb;Rps27a;Uba52
F
PISA: Q331K all vs WT all
destabilized proteins
Cluster 1
Cluster 2
Cluster 3
Cluster 4
Cluster 5
Cluster 6
Cluster 7
Rtraf
Prkce
Prkca
Myh10
Myh9
Dhx15
Cct6a
Tubb5
Pgk1
Usp5
Ddx1
Hspa4
Tcp1
Psmd6
Usp7
Cct8
Cct7
Rpl4
Rpl7
Rps18
Rpl3
Rpl12
Rpl18
Rpl13
Rpl26
Rpl36a
Npm1
Rpl13a
Atp5h
Rps6
Rps17
Rps8
Rps23
Rpl23a
Rpl24
Rpl10
Rps19
Rpl22
Ube2i
Rpl15
Rpl18a
Rpl34
Nisch
Fkbp1a
Rpl14
Rpl36

957

958 **Figure 6. PISA analysis identifies melting temperature shifts in ribosomal and chaperonin proteins**
959 **in Q331K mouse brain lysates. (A)** Top 10 gene set hits with GSEA enrichment of thermostability changes
960 in Q331K TBI versus WT TBI brain lysates using GOBP. Purple bars denote gene sets involved in ribosome
961 biology. **(B)** Heatmap showing levels of soluble protein detected by PISA for the top proteins in the pathway
962 "Cytoplasmic Translation". The $\log_2$(fold change) relative to the mean expression is shown for each sample.
963 **(C)** Box plot of top-ranking proteins in the "Cytoplasmic Translation" gene set for the indicated condition.
964 **(D,E)** Volcano plot for the quantitative proteomics (**D**) and PISA (**E**) results for Q331K ("Q331K All") versus
965 WT ("WT All"), where TBI and sham conditions are combined for each genotype to assess the main effects
966 of genotype while controlling for baseline differences related to injury. Ribosomal proteins are highlighted
967 as purple dots. (**F**) Results of a STRING analysis using the Markov Cluster Algorithm showing significantly
968 destabilized proteins (FDR < 0.1) in the "Q331K All" versus "WT All" comparison. Key terms included for
969 each cluster are as follows. Cluster 1: cytoplasmic translation, Signal Recognition Particle (SRP)-dependent
970 co-translational protein targeting to membrane, ribosome; Cluster 2: positive regulation of establishment of
971 protein localization to telomere, association of TriC/CCT with target proteins during biosynthesis, ATP-
972 dependent protein folding chaperone; Cluster 3, tRNA-splicing ligase complex; Cluster 4: Myosin II filament,
973 cell shape; Cluster 5: Nisch, Ube2i; Cluster 6: synthesis of active ubiquitin: roles of E1 and E2 enzymes;
974 Cluster 7: SHC-transforming protein 1 (SHC1) events in Erythroblastic Blast 2 (ERBB2) signaling, calcium-
975 dependent protein kinase C activity, presynaptic cystosol. String protein-protein interaction enrichment p-
976 value < $1.0e^{-16}$. Ribosomal proteins found to interact with TDP-43 in other studies are in bold within Cluster
977 1.(18, 91, 92)

978

979

980

981

982

983

984 the possibility that association of mutant TDP-43 with ribosomes and/or ribosomal proteins could
985 impact ribosome stability.(18, 91, 92) For the polysome profiling study, we noticed that the
986 absorbance at 254nm was consistently lower for Q331K cytosolic lysates relative to that of WT
987 within the peak where medium polysomes elute from the gradient (**Fig. S11B**). Additionally, we
988 observed a subpopulation of TDP-43 associating with the 80S ribosome (**Fig. S11C**). These
989 observations suggest that translation efficiency may be reduced in Q331K mouse brain relative
990 to WT mice. "Cluster 2", the second largest cluster revealed by STRING, includes multiple proteins
991 involved in protein folding such as heat shock 70 kDa protein 4 (Hspa4) and four of the eight
992 subunits that comprise the eukaryotic cytosolic T-complex protein 1 (TCP-1) ring complex or
993 chaperonin containing TCP-1 (TRiC/CCT), including Tcp1/Cct1, Cct6a, Cct7 and Cct8.
994 Interestingly, Cheng et al. identified these as putative TDP-43 interactors.(91) TRiC/CCT plays
995 important roles in maintaining proteostasis and ensuring the proper folding of critical cellular
996 proteins, lending further support to the notion that proteostasis-related processes are vulnerable
997 and dysregulated in mutant TDP-43 mice.(93)

998 There were 40 proteins that exhibited enhanced stabilization in Q331K versus WT cytosolic
999 lysates, although no cluster larger than 5 proteins was observed with STRING analyses and MCL
1000 clustering. Cluster 1 and 2 each contain 5 proteins associated with smooth muscle contraction
1001 and endocytosis, respectively (**Fig. S10G**). Interestingly, PISA detected four peptides derived
1002 from ubiquitin (**Fig. 6E**) with sequence homology shared amongst ubiquitin C, ubiquitin B,
1003 ubiquitin A-52 (Uba52) and Rps27a (**Supp. Table VI**). Uba52 and Rps27a are both ubiquitin-
1004 ribosomal fusion proteins.(94) Therefore, despite downregulation of proteostasis-related
1005 processes in Q331K mice at baseline, some compensatory mechanisms may be at play to
1006 overcome these adverse effects.

1007

1008

1009 **DISCUSSION**

1010 Herein, we show that expression of dysfunctional TDP-43 leads to deficits in multiple branches of
1011 the proteostasis network (**Fig. 7**). Proteostasis deficits occur independently of overt TDP-43
1012 overexpression, aggregation or mislocalization, which were not observed here or in prior reports
1013 describing this TDP-43 Q331K knock-in mouse model.(6, 44, 95) Analysis of our RNAseq
1014 datasets comparing Q331K and WT mice without brain trauma (i.e., naïve or sham conditions)
1015 revealed downregulation of genes involved in protein folding, including multiple heat shock
1016 proteins and chaperones, as well as genes involved in the ubiquitin proteosome pathway, such
1017 as *Gid4* and *Spop*. Exon skipping of *Ube3c*, an RNA target of TDP-43 that encodes an E3 ubiquitin
1018 ligase, was also detected in brain lysates from Q331K mice. This gain of TDP-43 mis-splicing
1019 function was initially reported in TDP-43 mouse strains with endogenous mutations in the low
1020 complexity domain, including a Q331K variant.(82) Although changes in *Ube3c* expression levels
1021 were not detected by RNAseq, AlphaFold and PyMol analyses predict that mis-splicing of *Ube3c*
1022 could alter the structure of Ube3c near the ubiquitin-binding domain. Further, Fratta et al. reported
1023 that about 15% of the exon skipping events identified in mutant TDP-43 mice occurred in genes
1024 within the ubiquitin proteosome pathway.(82) A decrease in proteosome-encoding transcripts
1025 early in life is a predictor of shortened lifespan in killifish, a vertebrate model used for aging
1026 studies.(96) Together, these observations support the notion that dysfunctional TDP-43 adversely
1027 affects the quality control arm of the proteostasis network, which in turn correlates with a decline
1028 in health and life-expectancy.

1029

1030 PISA, a novel approach for identifying alterations in biological complexes through thermostability
1031 measurements,(86, 87) further highlighted protein folding as a vulnerable component of the
1032 proteostasis network in Q331K mice, where multiple proteins within the essential molecular
1033 chaperone TRiC/CCT were found to be destabilized. Further, 20 out of 79 core ribosomal proteins
1034 were found to exhibit reduced thermal stability through our PISA analysis.(97) These data suggest

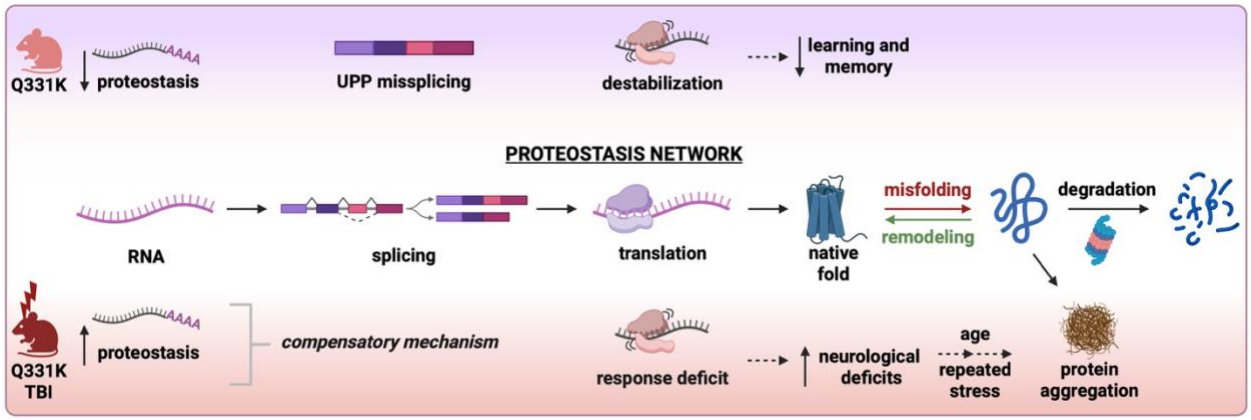

Figure 7. Proposed model for how the proteostasis network is affected by TDP-43 dysfunction. The proteostasis network is illustrated in the center of the diagram. Under baseline conditions (top), genes involved in proteostasis and the ubiquitin-proteasome pathway (UPP) are downregulated and mis-spliced in Q331K mouse brain relative to WT mice. In Q331K mouse brain lysates, ribosomal proteins are destabilized, which may compromise protein synthesis and thus contribute to the cognitive deficits observed in Q331K mice. In response to CNS challenge in form of a TBI (bottom), compensatory mechanisms appear to be activated in Q331K mice, including an upregulation of proteostasis-related genes at the RNA level. However, Q331K mice fail to mount a physiological response to TBI, as demonstrated by worse neurological deficits and delayed recovery after brain injury compared to their WT counterparts. We posit that destabilization of ribosomal proteins and chaperone complexes involved in proteostasis underlies the enhanced neurological deficits exhibited by Q331K mice after TBI. Although Q331K mice ultimately recover from TBI, we predict that repeated CNS challenge as a function of aging will exacerbate the phenotypes uncovered herein, and could lead to neurodegeneration and pathological TDP-43 aggregation. Model figure generated with BioRender.

1056 that complexes formed by ribosomal proteins, namely ribosomes, could be affected by expression
1057 of dysfunctional TDP-43 in a manner that compromises this macromolecular complex (**Fig. 7**).
1058 TDP-43 has been shown to associate with ribosomal proteins through co-immunoprecipitation
1059 and proximity labeling experiments,(18, 48, 91, 92) and with actively translating ribosomes in
1060 cultured cells.(47, 48) Ribosomal proteins have also been detected within pathological TDP-43
1061 aggregates(48, 98) and in amyloid-positive aggregates within the aging brain.(96) In various
1062 contexts, TDP-43 expression can either repress or activate protein synthesis.(49, 50)
1063 Interestingly, the association of TDP-43 with translation-related factors can be modulated by the
1064 phase-separation behavior of TDP-43.(18) Proper phase separation of TDP-43 in vitro and in vivo
1065 requires residues 321-340, referred to as the conserved region (CR).(17-19) Deletion of the CR
1066 resulted in enhanced interactions between TDP-43 and translation factors together with
1067 heightened rates of global protein synthesis in vivo.(18) While the Q331K variant studied herein
1068 also reportedly disrupts TDP-43 phase separation,(17, 19) our polysome profiling data suggest
1069 that translation efficiency is reduced in Q331K mouse brain relative to WT brain. Therefore, there
1070 may be differential effects of the CR on translational regulation depending on how the TDP-43
1071 sequence is modified (i.e., deletion versus single point mutation). We note that PISA was
1072 performed on organelle-depleted brain lysates in this study, such that changes to nuclear and
1073 mitochondrial proteins would not have been captured in this analysis. Indeed, it will be interesting
1074 to extend PISA for analysis of other cellular compartments and organelles in future studies.
1075
1076 It remains to be determined precisely how expression of mutant Q331K in mice leads to reduced
1077 thermostability of ribosomal proteins. Disease-linked mutations may perturb interactions between
1078 TDP-43 and ribosomal proteins,(91) which could induce conformational changes within the
1079 ribosome (**Fig. 7**), other complexes that include ribosomal proteins and/or free ribosomal
1080 proteins.(99) Ribosomal protein stability could also be indirectly affected by mutant TDP-43
1081 expression. For example, altered proteostasis, activation of stress-response pathways and other

1082 stimuli can affect the post-translational modification status of ribosomal proteins, which may
1083 impact ribosome conformation and activity.(100) Intriguingly, ribosomal proteins underwent a shift
1084 toward enhanced stability in WT animals after TBI, possibly representing a mechanism that
1085 protects these proteins during cellular stress.(101) Although we do not observe changes in overall
1086 levels of ribosomal proteins in WT or Q331K mice, expression of mutant TDP-43 could influence
1087 the stoichiometry of ribosomal proteins, if not at the age of mice studied here (i.e., 16 weeks),
1088 potentially in older mice. The stoichiometry of ribosomes is reportedly compromised during aging,
1089 possibly a side-effect of impaired proteosome activity, which may lead to an accumulation of
1090 "orphan" ribosomal proteins that are prone to aggregate.(96, 101) TDP-43 dysfunction has also
1091 been linked to deficits in transporting mRNAs that encode ribosomal proteins(102) and in the
1092 stability of ribosome-encoding transcripts,(103) both of which could also impact ribosome integrity
1093 and protein translation.(49, 50) Deficiencies in protein synthesis may contribute to some cognitive
1094 deficits observed in Q331K mice,(44) including attenuated cue-induced freezing in the CCFC test
1095 in Q331K mice prior to surgery.(69) Although TBI is known to induce translational repression,
1096 upregulated expression of select proteins is thought to be important for mitigating the effects of
1097 trauma.(104) Our data support a model whereby Q331K mice are unable to mount a physiological
1098 response to TBI due to multiple deficits within the proteostasis network that likely include deficits
1099 in protein synthesis and folding (**Fig. 7**).
1100
1101 In addition to TBI,(13, 37-41) TDP-43 has been linked to other stress-related pathways in vitro(2-
1102 6, 11, 12) and in vivo.(15, 78). That TDP-43 undergoes a change in subcellular localization in
1103 response to a broad range of stressors suggests TDP-43 may serve as a general stress-sensor,
1104 a notion supported by our observation that TDP-43 re-distributes to the cytoplasm under
1105 conditions of sham surgery. Stress-induced subcellular re-distribution of TDP-43 is modulated by
1106 TDP-43 RNA-binding capacity and TDP-43 post-translational modification status, and this
1107 redistribution can coincide with mis-splicing signatures corresponding to TDP-43 loss of

1108 function.(3, 4, 7-9, 105) Here, we observe robust TBI-induced changes in subcellular TDP-43
1109 localization in both WT and Q331K mouse brain tissue, including a ring-like TDP-43 staining
1110 pattern that has not been widely reported. Changes in TDP-43 localization were most prominent
1111 in the hypothalamus and the amygdala, the latter region having been linked to behavioral
1112 dysfunction in human sporadic ALS.(106) *A priori*, we expected TBI-induced changes in TDP-43
1113 localization to coincide with splicing defects associated with TDP-43 loss-of-function.(4, 9, 82,
1114 105) However, the splicing patterns of known TDP-43 targets were primarily influenced by TDP-
1115 43 mutation and largely unaffected by TBI. It is possible that emerging reporters of TDP-43-
1116 mediated cryptic splicing could be more sensitive for detection of TDP-43 loss-of-function in cells
1117 with altered TDP-43 localization in our TBI model.(107)
1118
1119 The outcomes of our study lend support to the hypothesis that ALS pathogenesis occurs through
1120 a multistep process, where steps may represent genetic, environmental and/or behavioral risk
1121 factors.(34, 35) Notably, we detected a synergistic effect of TDP-43 mutation and TBI on gene
1122 expression profiles that are relevant to ALS pathogenesis. Indeed, there is substantial overlap in
1123 GSEA hallmark gene sets in CNS tissues between Q331K TBI mice 24h post-TBI and human
1124 post-mortem ALS/FTLD-TDP cases,(45, 46) even though the Q331K TBI mice eventually recover,
1125 and the human cases represent end-stage disease. Our interpretation is that expression of mutant
1126 TDP-43 causes mice to become vulnerable to CNS challenge, resulting in dysregulation of key
1127 biological pathways that are also dysregulated during ALS/FTD pathogenesis. In Q331K mice,
1128 TBI-induced phenotypes that were observed 24h post-TBI, such as exaggerated neurological
1129 deficits (i.e., higher NSS), proteostasis-related gene upregulation, changes in *Ube3c* splicing and
1130 subcellular TDP-43 re-distribution, were largely restored to baseline levels 5-7 months post-TBI,
1131 consistent with this being a mild model of TBI.(43). Further, compensatory mechanisms, such as
1132 an upregulation of proteostasis-related genes, appear to be activated in Q331K mice (**Fig. 7**).
1133 Despite these protective measures, Q331K mice exhibited worse neurological outcomes in the

1134 acute phase post-TBI, indicating that stress-related pathways were vulnerable to dysfunctional
1135 TDP-43. This notion is further supported by a recent study demonstrating reduced stress granule
1136 formation in mutant TDP-43 mice exposed to hyperthermia.(15) We posit that repeated incidence
1137 of TBI and/or exposure to additional risk factors would lead to pathological and chronic
1138 degenerative phenotypes that persist months after the injury occurs (**Fig. 7**). Mathematical
1139 modeling of incidence data for human ALS cases with TDP-43 mutation indicated that disease
1140 pathogenesis may require up to five steps, where only one step is attributed to TDP-43
1141 mutation.(34, 35) In the case of sporadic ALS, six steps are predicted for disease pathogenesis.
1142 Accordingly, environmental and behavioral risk factors likely play a significant role in ALS
1143 pathogenesis.(32, 33) While the TDP-43 Q331K mutation represents one step in the current
1144 study, TDP-43 dysfunction can also manifest in the absence of genetic mutations. For example,
1145 altered post-translational and transcriptional forms of TDP-43 that have been detected in sporadic
1146 ALS cases have also been linked to TDP-43 dysfunction.(108, 109)
1147

1148 **Conclusions**

1149 Outcomes of this study demonstrate that expression of dysfunctional TDP-43 predisposes mice
1150 to worse neurological outcomes following brain trauma. Deficiencies in multiple branches of the
1151 proteostasis network likely contribute to this vulnerability of mutant TDP-43 mice to TBI (**Fig. 8**).
1152 Therefore, targeting the proteostasis network should be a viable therapeutic direction for treating
1153 TDP-43 proteinopathies. For example, proteostasis could be enhanced by mitigating protein
1154 misfolding and stress through activation of heat-shock proteins and chaperones.(110) TDP-43
1155 dysfunction can manifest through both genetic and non-genetic causes, where mutant TDP-43
1156 expression altered the physiological response to TBI herein. We predict that TDP-43 dysfunction
1157 will similarly affect cellular response and recovery pathways associated with other forms of CNS
1158 challenge.(15) Further, repeated and/or additional incidences of CNS challenge are expected to
1159 increase the likelihood of developing a TDP-43 proteinopathy such as ALS (**Fig. 8**).

1160 **List of abbreviations**

Abbreviation	Description
AD	Alzheimer's disease
ALS	amyotrophic lateral sclerosis
BCA	bicinchoninic acid
BSA	bovine serum albumin
Calr	calreticulin
CCFC	cued and contextual fear conditioning
CR	conserved region
CTE	chronic traumatic encephalopathy
Dnajc5	DnaJ heat shock protein family (Hsp40) member 5
ER	endoplasmic reticulum
ES	enrichment score
FOV	field of view
FTD	frontotemporal dementia
FTLD	frontotemporal lobar degeneration
Gid4	glucose-induced degradation protein 4 homolog
GO	gene ontology
GOBP	Gene Ontology Biological Process
GSEA	Gene Set Enrichment Analysis
GT	genotype
HECT	homologous to the E6-AP Carboxyl Terminus
Hspa4	heat shock 70 kDa protein 4
IACUC	Institutional Animal Care and Use Committee
IDR	intrinsically disordered region
INJ	Injury (i.e. sham or TBI)
Kcnip2	potassium voltage-gated channel interacting protein 2
LATE	limbic-predominant age-related TDP-43 encephalopathy
LC-MS/MS	liquid chromatography tandem mass spectrometry
Manf	mesencephalic astrocyte-derived neurotrophic factor
MCL	Markov Clustering
MSigDB	molecular signatures database
MTOR1	mammalian target of rapamycin complex 1
N/C	nuclear-to-cytoplasmic
NES	normalized enrichment score
NMDA	N-methyl-D-aspartate
NSS	neurological severity score
Pacrgl	parkin coregulated like

PCA	principal component analysis
Pdia3	protein disulfide isomerase family A, member 3
Pdia6	protein disulfide isomerase family A, member 6
PFA	paraformaldehyde
PISA	proteome integral solubility alteration
Ppp3ca	protein phosphatase 3 catalytic subunit alpha
pre-mRNA	pre-messenger RNA
PSM	peptide-spectrum match
PVDF	polyvinylidene fluoride
RNA-seq	bulk RNA-sequencing
RNP	ribonucleoprotein
Rplp1	large ribosomal subunit protein P1
Rps27a	ribosomal protein S27a
RT-PCR	Reverse transcription polymerase chain reaction
Slc6a6	solute carrier family 6 member 6
Sort1	Sortilin-1
Spop	speckle-type POZ protein
Ssr1	signal sequence receptor subunit 1
TAMC	Transgenic Animal Modeling Core
TBI	traumatic brain injury
TCP-1	cytosolic T-complex protein 1
TDP-43	TAR DNA-binding protein 43
TMT	tandem mass tag
TRiC/CCT	eukaryotic TCP-1 ring complex or chaperonin containing TCP-1
Tsn	translin
Uba52	ubiquitin A-52
Ube3c	ubiquitin protein ligase E3C
UPLC	UltraPerformance LC
WT	wild-type
Xbp1	active X-box binding protein 1
Xbp1s	spliced active X-box binding protein 1
Xbp1u	unspliced active X-box binding protein 1

1166 **Declarations**

1167 **Ethics approval and consent to participate.** Not applicable.

1168 **Consent for publication.** Not applicable.

1169 **Availability of data and materials.** Mass spectrometry proteomics data are available via
1170 ProteomeXchange with identifier PXD068825 and 10.6019/PXD068825.Submission of RNAseq
1171 dataset to GEO are in progress at the time of this manuscript submission.

1172 **Competing interests.** The authors declare that they have no competing interests

1173 **Funding.** This work was supported by CDMRP/DoD DOD/W81XWH-20-1-0271 (D.A.B and N.H),
1174 the Angel Fund for ALS Research (D.A.B and N.H.), NINDS R21NS139100 (D.A.B.), and the First
1175 Affiliated Hospital of Chongqing Medical University (J.Z.).

1176 **Authors' contributions. MSR** performed all the mass spectrometry experiments and analyzed
1177 the resulting data, performed most of the RNAseq analyses and was a major contributor in writing
1178 and preparing the manuscript; **MFM** performed the TDP-43 localization analyses, contributed to
1179 the RNA-related analyses, and created multiple figures in the manuscript; **JZ** performed animal
1180 surgeries, performed the CCFC analyses, and acquired the confocal microscopy images; **KO**
1181 performed the RT-PCR analyses; **EAW** isolated RNA from mouse tissue and coordinated the
1182 RNA sequencing and provided some assistance in the analysis; **DC** maintained the mouse colony
1183 and assisted in the animal studies; **KS** assisted in the animal studies and performed
1184 immunofluorescence; **JB** performed the NSS tests and helped with surgeries; **HM** performed the
1185 AlphaFold analyses and contributed to the RT-PCR analyses; **MNA** performed the polysome
1186 profiling studies together with MSR; **FM** performed the PyMOL analyses and interpreted the
1187 results; **ART** and **SM** assisted in the CCFC study; **JAN** assisted with confocal microscopy; **NH**
1188 contributed to the experimental design for the TBI surgeries and analyzed the animal behavior
1189 data; **ODK** performed the tests of differential gene expression for the RNAseq data and was a

major contributor to the omics analyses. **DAB** conceived and directed the project, analyzed data and wrote the manuscript with contributions from co-authors.

Acknowledgements. We are grateful for services provided by UMass Chan core facilities including the Transgenic Animal Modeling Core, Mouse Behavioral Core, Mass Spectrometry Facility and Molecular Biology Core Labs. We thank Dr. Joel Richter for use of equipment and advice related to polysome profiling; Drs. Patrick Sullivan, Hemendra Vekaria, Myriam Heiman, Jack Humphrey, Sami Barmada, Christine Vande Velde and Clotilde Lagier-Tourenne and members of their labs for valuable advice; and current and former members of Bosco lab, especially Dr. Ozge Yildiz and Jonathan Jung for help on this project.

Authors' information. Not applicable.

1216 **Additional file 1. Supplemental Figures (Fig. S1 thru S11)**

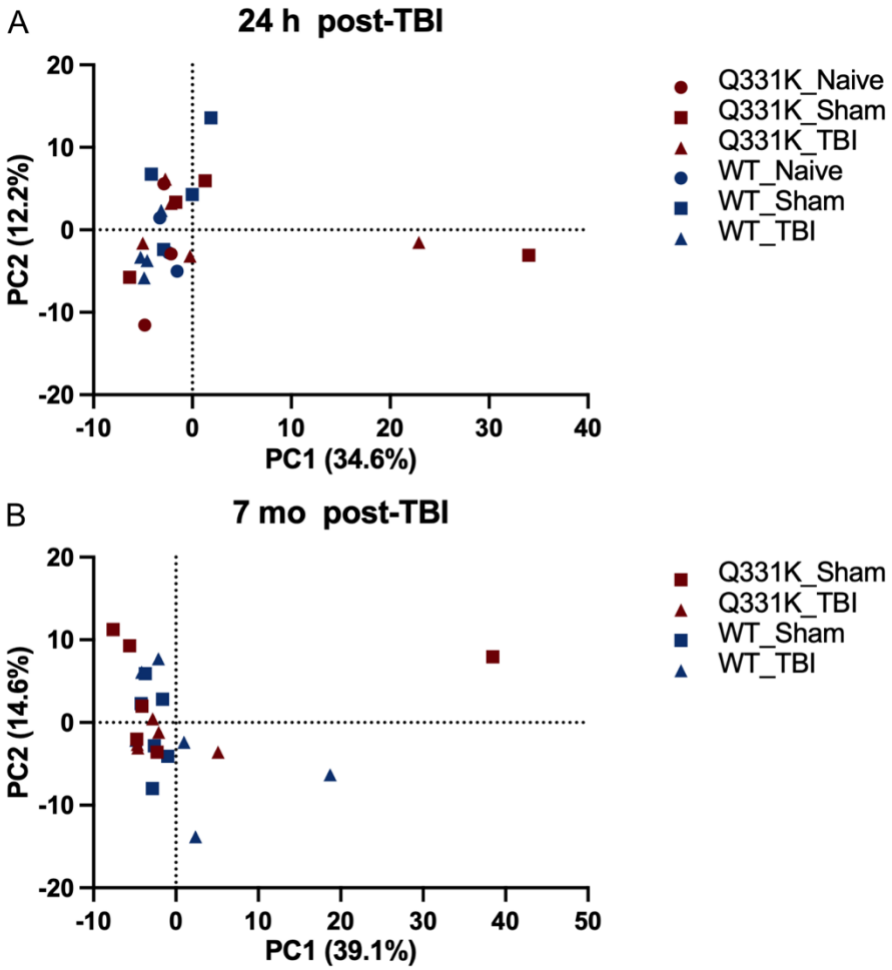

1217
1218 **Figure S1. Principal component analysis (PCA) identifies outliers in RNAseq datasets.** PCA analysis using 1000
1219 genes with the highest variance for the 24 h post-TBI **(A)** and 7 mo post-TBI (**B**) datasets. Genes were selected based
1220 on their variance (sigma^2) after adjusting for the mean-variance trend by fitting the expression data with the limma
1221 functions voom and lmFit, both using a design with a single group.
1222
1223
1224
1225
1226
1227
1228

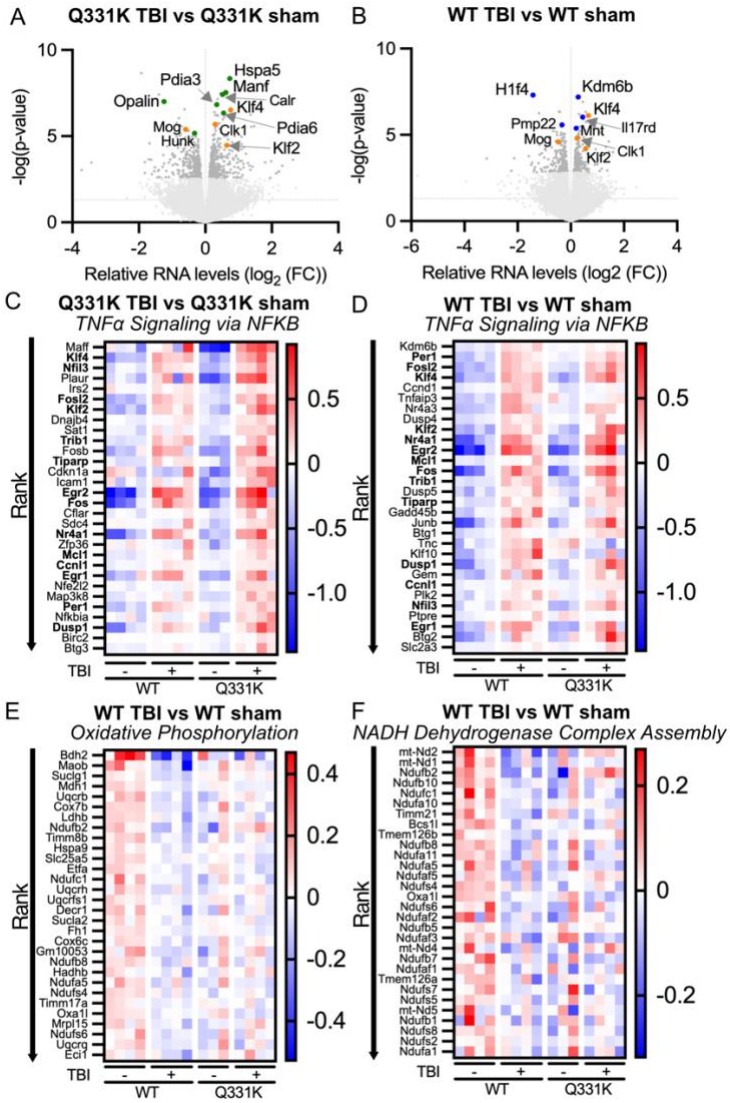

Figure S2. Overlapping and differential gene expression profiles in WT versus Q331K mice after TBI. (A) Volcano plot of transcriptional changes from RNAseq analyses for Q331K mice under conditions of TBI versus sham surgery. **(B)** Volcano plot of transcriptional changes from RNAseq analyses for WT mice under conditions of TBI versus sham surgery. **(A,B)** Hits with FDR <0.1 are shown in red. Orange dots highlight top gene hits (*Klf2*, *Klf4*, *Mog*, *Clk1*) resulting from TBI, irrespective of genotype. Blue dots denote top gene hits specifically in the WT TBI condition whereas green dots are top gene expression changes specifically in the Q331K TBI condition. **(C,D)** Heatmap showing the top 30 ranked genes in the top up-regulated gene set for hallmark "TNFalpha signaling via NFKb" for Q331K TBI versus Q331K sham (C) and WT TBI versus WT sham (D). Fourteen genes (in bold) are significantly altered under "TNFalpha signaling via NFKb" for both the Q331K TBI and WT TBI conditions relative to their respective sham group. **(E,F)** Heatmap showing the top 30 ranked genes in the top down-regulated gene set in hallmark collection, "Oxidative Phosphorylation" (E), and Gene Ontology Biological Process collection, "NADH Dehydrogenase Complex Assembly" (F), for the WT TBI versus WT sham comparison. The $\log_2$(fold change) relative to the mean expression is shown for each sample.

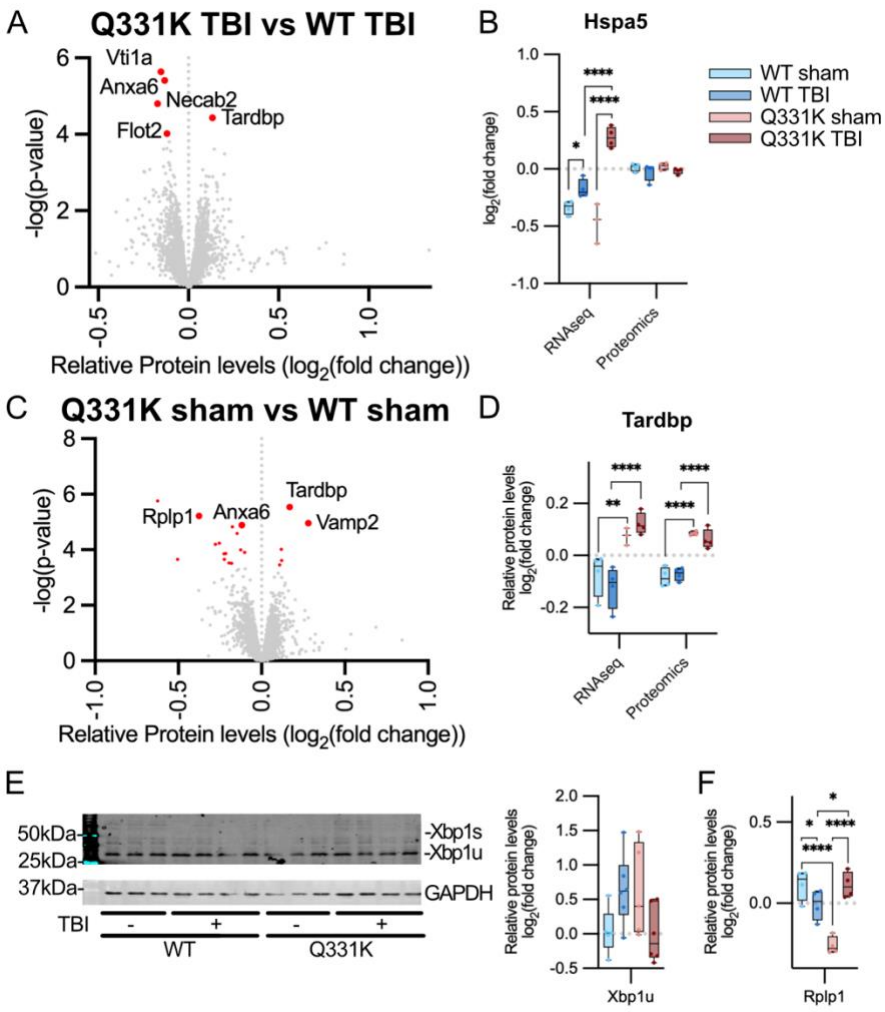

Figure S3. Proteomic analyses identify protein changes altered by TBI and mutant TDP-43 genotype. (A) Volcano plot showing relative protein level changes between Q331K TBI and WT TBI cohorts. Hits with FDR <0.1 are highlighted in red. **(B)** Hspa5 is unchanged at the protein level by quantitative proteomics. **(C)** Volcano plot showing relative protein level changes between Q331K sham and WT sham cohorts. Hits with FDR <0.1 are highlighted in red. **(D)** Tardbp is significantly elevated in Q331K mouse brain by transcriptomics and proteomics analyses. **(E)** Total levels of Xbp1 are unchanged and there is no detection of spliced Xbp1 by Western analysis. The expected molecular weight of spliced Xbp1 (Xbp1s) is 54 kDa and of unspliced Xbp1 (Xbp1u) is 29 kDa. Note, the band located at ~35 kDa is nonspecific. **(F)** Protein levels of Rplp1 as determined by quantitative proteomics. Nominal p-value = * <0.05; **<0.01, ****<0.0001.

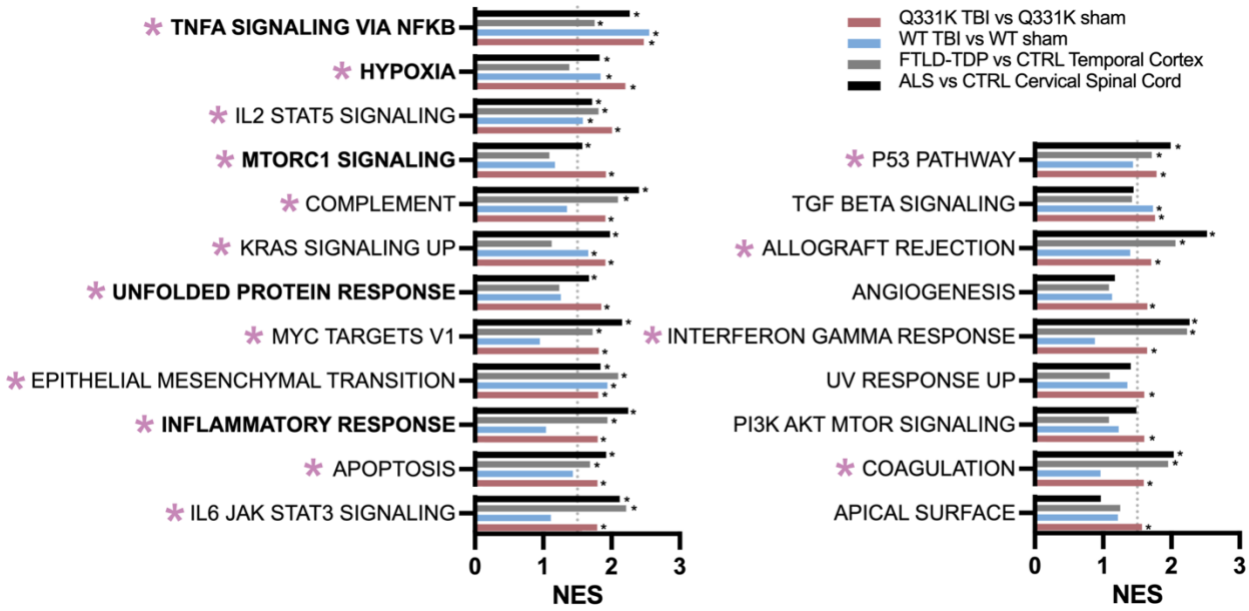

Figure S4. Comparison of published human ALS and FTLD post-mortem datasets with current TBI mouse study. Directional p-values were calculated from published datasets reported in Humphrey et al,(46) and Hasan et al (45) and subjected to GSEA using the hallmark database as described in methods for RNAseq. Asterisks to the right of the bars denote FDR<0.05 for the indicated comparison defined in the key. The dotted line indicates NES of 1.5. Gene sets with a pink asterisk highlight those that are significant for the Q331K TBI versus Q331K sham comparison (pink bars), and at least one of the human datasets (grey and black bars). There are 16/21 gene sets that meet this criterion, and only 5/21 gene sets that are significant for the WT TBI versus WT sham comparison (blue bars) and at least one of the human datasets. Gene set names in bold are discussed in the main text.

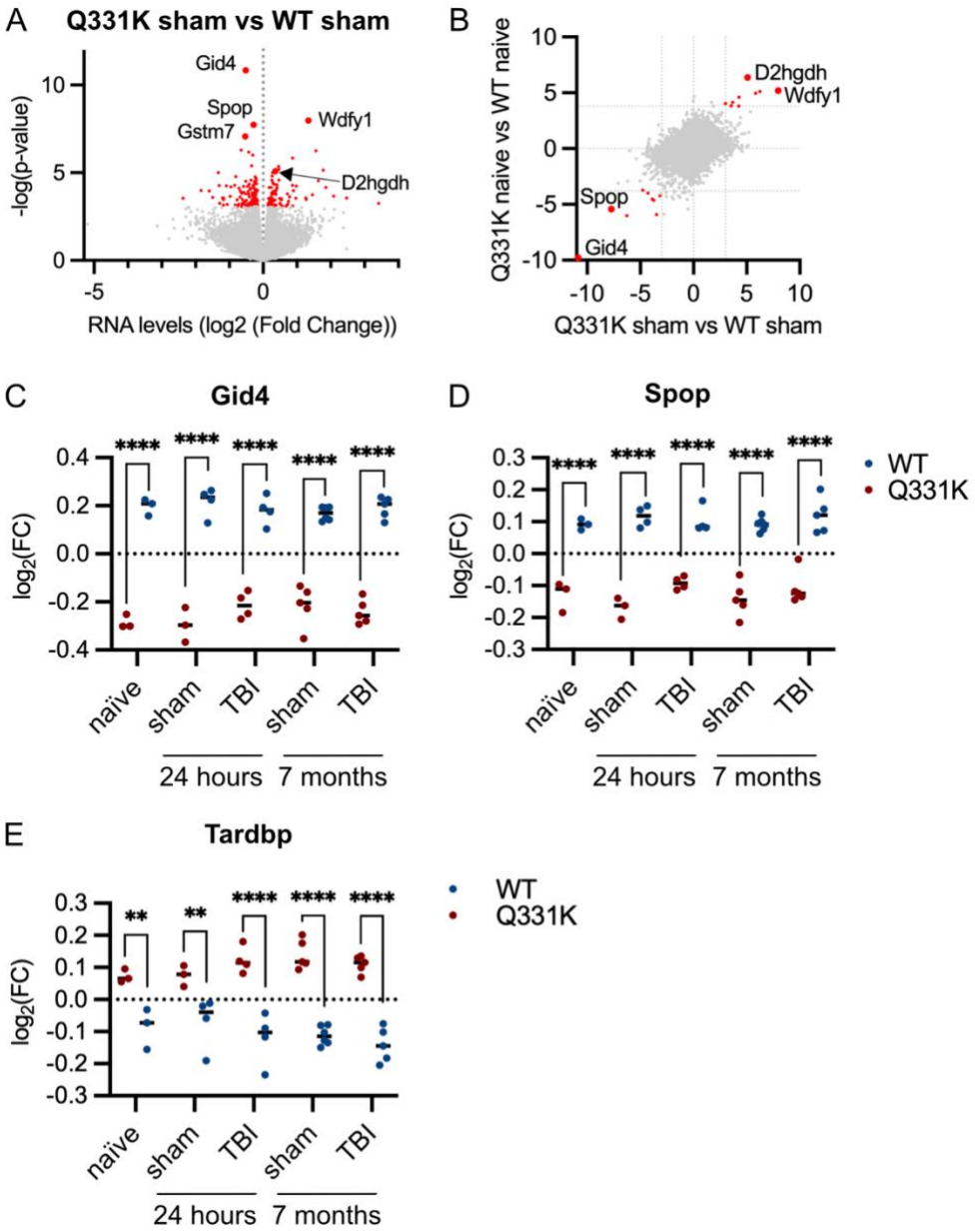

Figure S5. Omics analyses identify Q331K-specific changes to the transcriptome (A) Volcano plot with the significant up- and down-regulated transcripts in red for the Q331K sham versus WT sham comparison. **(B)** Directional p-value plot overlaying the Q331K sham versus WT sham datasets with the Q331K naive versus WT naive datasets to identify reproducible mutant TDP-43-specific changes, which are highlighted in red. Directional p-value = $-\log_{10}$(p-value)*sign of $\log_2$(fold change) **(C-D)** Plots of the most significant Q331K-specific down-regulated genes, *Spop* and *Gid4*, which are both involved in the ubiquitin-proteosome pathway. **(E)** Elevated *Tardbp* is observed in all Q331K vs WT comparisons. For C-E, time post-surgery is indicated below. Nominal p-value = **<0.01, ****<0.0001.

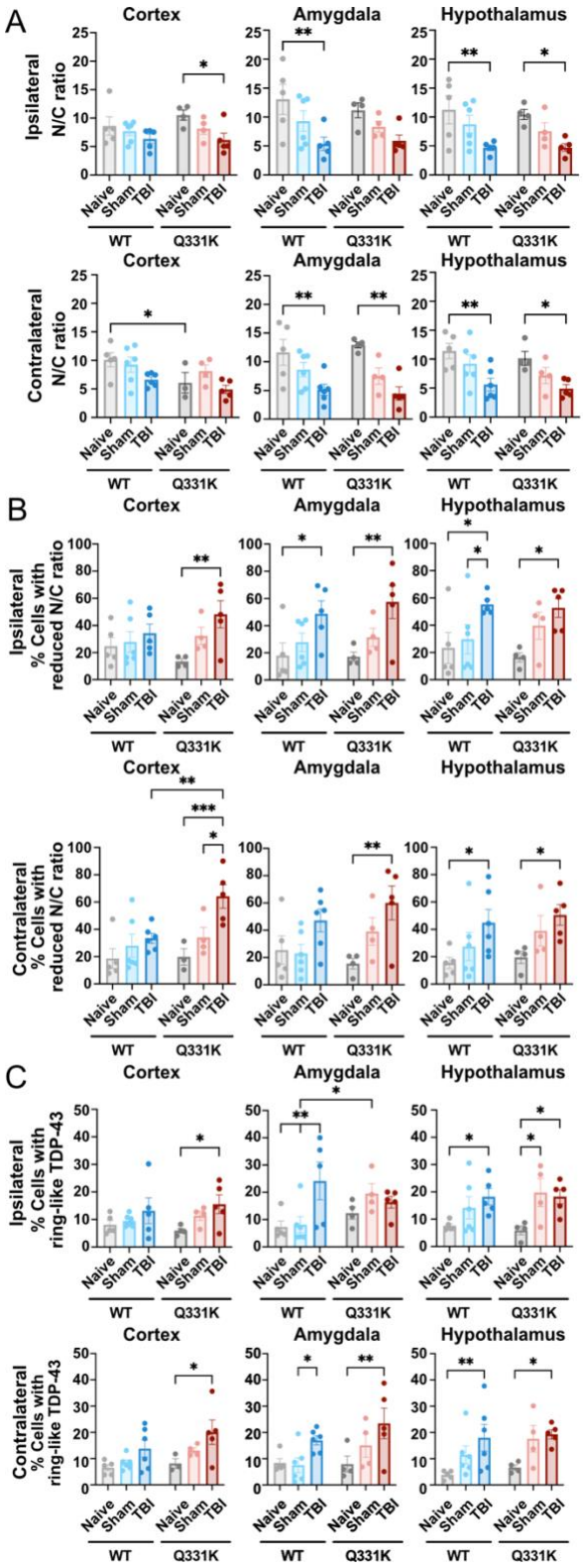

Figure S6. Changes in TDP-43 subcellular localization in mouse brain tissue 24h post-surgery. (A) Nuclear-to-cytoplasmic (N/C) ratio of TDP-43 signal in naïve mice or 24h post-surgery (sham or TBI) mice determined from immunofluorescence analysis of tissue sections from the cortex (left), amygdala (middle), and hypothalamus (right), either ipsilateral (top) or contralateral (bottom) to the TBI site. **(B)** Percent of cells that exhibit reduced TDP-43 N/C ratios in the tissues from (A). **(C)** Percent of cells that exhibit "ring-like" TDP-43 distribution in the tissues from (A). Each dot represents data from an individual mouse, with n=4-6 mice per cohort. Statistics was performed using two-way ANOVA followed by Tukey's multiple comparisons test between conditions. *p<0.05, **p<0.01, ***p<0.001, ****p<0.0001

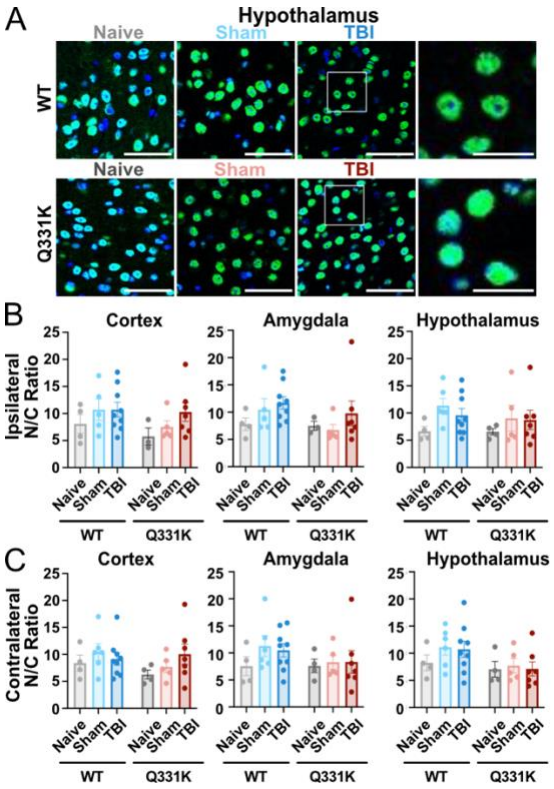

Figure S7. Lack of significant TDP-43 subcellular alteration in mouse brain tissue 5 months post-surgery. (A) Confocal immunofluorescence images of hypothalamus brain sections from WT and Q331K mice, either without surgery (naïve) or 5-months post-surgery (sham or TBI). Sections are stained for TDP-43 (green) and counterstained with DAPI (blue). Scale bars=20 um. **(B,C)** Quantification of the nuclear-to-cytoplasmic (N/C) ratio of TDP-43 signal in WT and Q331K mice 5-months post-surgery in the cortex, amygdala and hypothalamus, either ipsilateral (B) or contralateral with respect to the impact site. Each dot represents data from an individual mouse, with n=4-9 mice per cohort. Statistics was performed using two-way ANOVA followed by Tukey's multiple comparisons test between conditions.

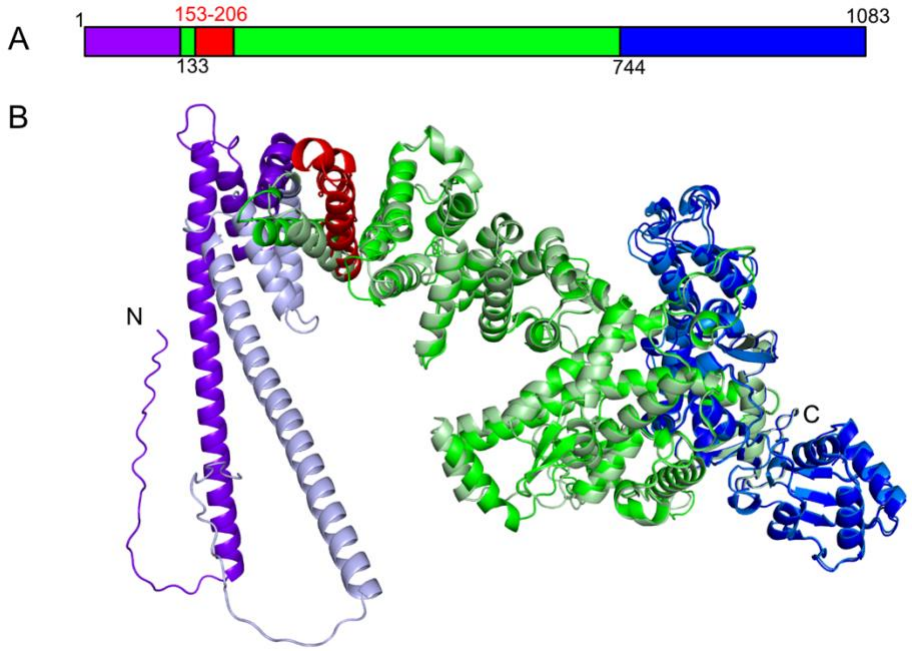

1335

1336 **Figure S8. Structural analysis of TDP-43-relevant splice variants using AlphaFold and PyMOL. (A)** Schematic
1337 representation of the ubiquitin-protein ligase E3C (Ube3c) protein highlighting distinct domains. Residue numbers are
1338 indicated at the start of each domain. The ubiquitin-binding domain (residues 1–132) is shown in purple, the second
1339 domain (residues 133–743) in green, and the catalytic Homologous to the E6-AP Carboxyl Terminus (HECT) domain
1340 (residues 744–1083) in blue. Residues corresponding to exon 6 (residues 153–206) are highlighted in red. **(B)** Overlay
1341 of AlphaFold-predicted structures for Ube3c containing exon 6 (domains in purple, green, and blue) with the predicted
1342 structures for Ube3c lacking exon 6 (domains in light purple, light green, and light blue). Structural alignments were
1343 performed in PyMOL, yielding an RMSD of 2.3 Å for alignment of only the ubiquitin-binding domain and an RMSD of
1344 8.5 Å for the entire protein.

1345

1346

1347

1348

1349

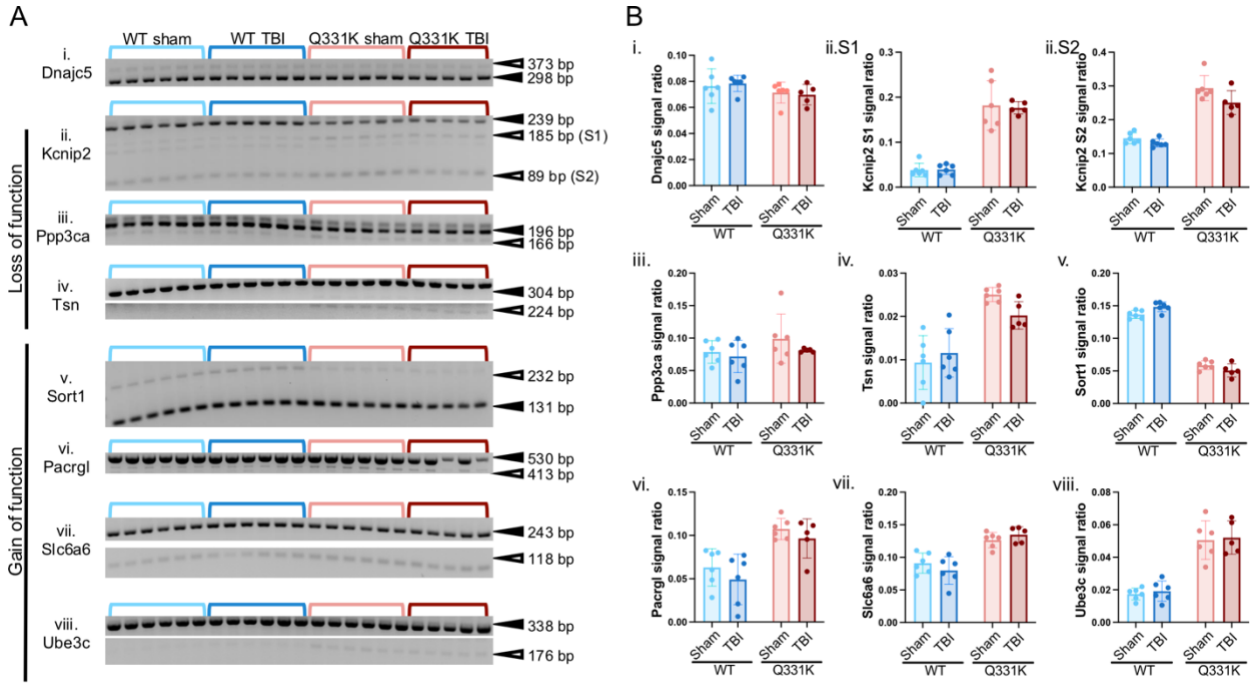

Figure S9. Alternative splicing targets of TDP-43 in WT and Q331K mice at 7 months post-injury. (A) Splice variants of known TDP-43 RNA targets (i-vi) detected by RT-PCR analysis in WT and Q331K mice 24h after either TBI or sham surgery. The PCR primers, exons of interest and references for the primers used in this study are shown in **Supp Table VI**. Splicing patterns that are consistent with TDP-43 loss of function or gain of function are indicated. Common and mis-spliced variants are denoted by, respectively, closed and open arrowheads with the corresponding size (bp=base pairs) of the PCR product. **(B)** Densitometry analysis of the gels in (A) was used to determine the ratio of the mis-spliced/common PCR product for each gene of interest. Each dot in the graph represents a separate mouse.

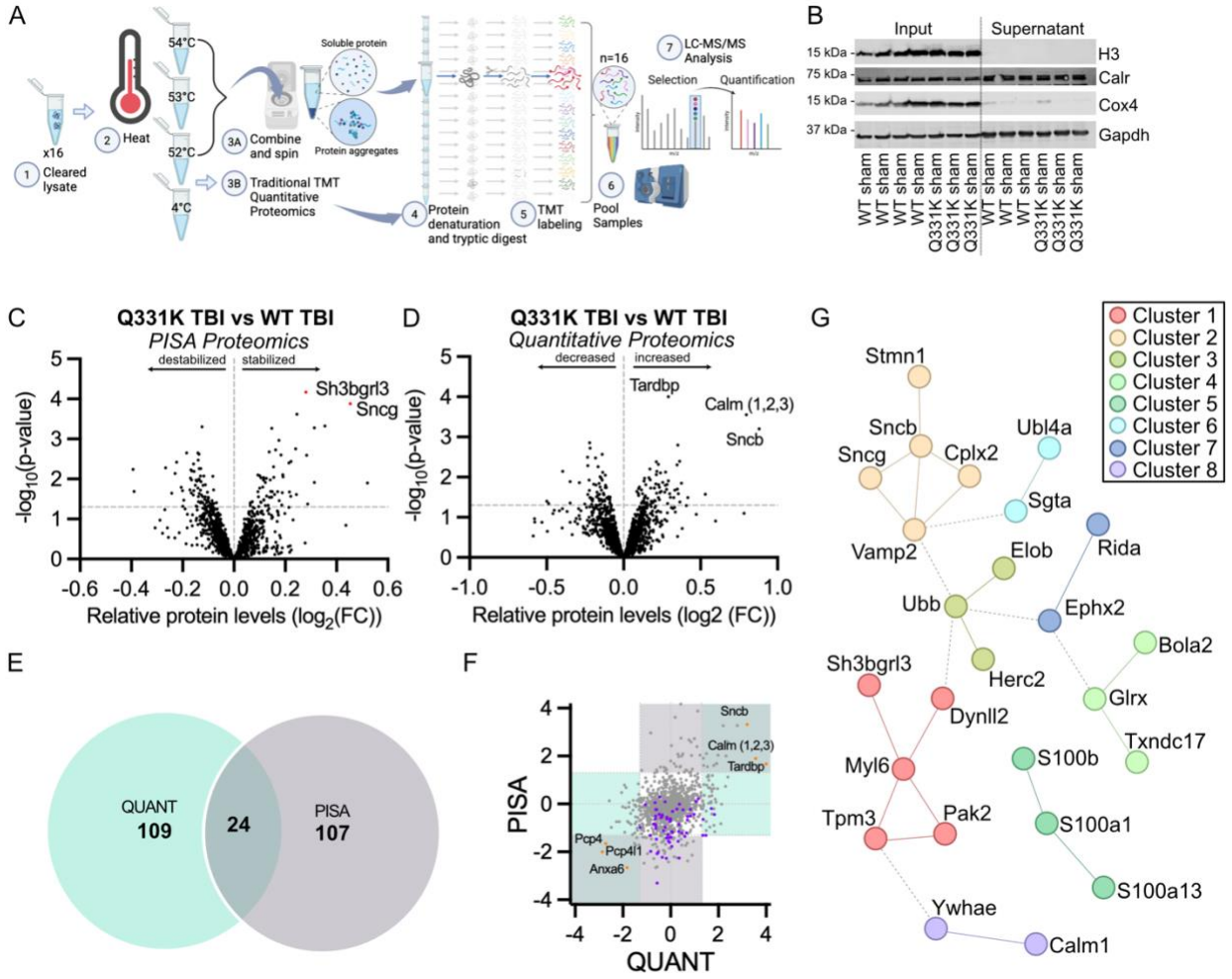

Figure S10. Quantitative proteomics of organelle-depleted cytoplasmic brain lysates. (**A**) PISA protocol for identifying proteins with altered thermostability between conditions: (1) Lysates are generated with mild, non-denaturing conditions and homogenization. Lysates are cleared by centrifugation. (2) Each sample is divided into four samples, where one is placed on ice for traditional quantitative proteomics and three are subjected to heat for protein denaturation. (3A) Aggregated protein is removed by centrifugation. (3B) The sample for traditional TMT quantitative proteomics remains on ice while samples for PISA are heated. (4) The soluble protein is digested with trypsin and labeled (5) with isobaric TMTpro-18plex tags. (6) Tagged samples are pooled, generating two sample sets (one from PISA and one from traditional quantitative proteomics) and subjected to mass spectrometry for quantification (7). Created with biorender.com. (**B**) Western analyses of organelle depleted supernatant (supernatant) compared to the whole brain sample input (input). (**C-D**) Volcano plot of protein changes identified by traditional quantitative proteomics (**C**) and PISA (**D**) for Q331K TBI versus WT TBI conditions. (**E**) Overlapping hits between quantitative proteomics and PISA are assessed to distinguish protein level changes from thermostability changes. (**F**) Directional p-value plot of Q331K TBI versus WT TBI for PISA and QUANT (quantitative proteomics). Purple dots indicate ribosomal proteins.

1376 Orange dots are highlighting top hits found in both PISA and QUANT. (**G**) Clustering using the Markov Cluster Algorithm
1377 for "Q331K All" versus "WT All" (defined in Figure 7 legend) for the stabilized proteins passing FDR adjustment (FDR
1378 <0.1). Only proteins identified as part of a cluster are shown. Cluster 1: Smooth Muscle Contraction; Cluster 2: Synaptic
1379 vesicle endocytosis, Synaptobrevin 2-SNAP-25-syntaxin-1a-complexin II complex; Cluster 3: Inactivation of
1380 Granulocyte colony-stimulating factor (G-CSF) signaling; Cluster 4: Protein-disulfide reductase nicotinamide adenine
1381 dinucleotide phosphate (NAD(P)) activity; Cluster 5: S-100/Intestinal calcium-binding protein (ICaBP) type calcium
1382 binding domain; Cluster 6: ER membrane insertion complex; Cluster 7: Epoxide hydrolase 2 (Ephx2), reactive
1383 intermediate imine deaminase A (Rida); Cluster 8: Negative regulation of calcium ion export across plasma membrane.
1384 Protein-protein interaction enrichment p-value = $2.94e^{-06}$.
1385
1386
1387

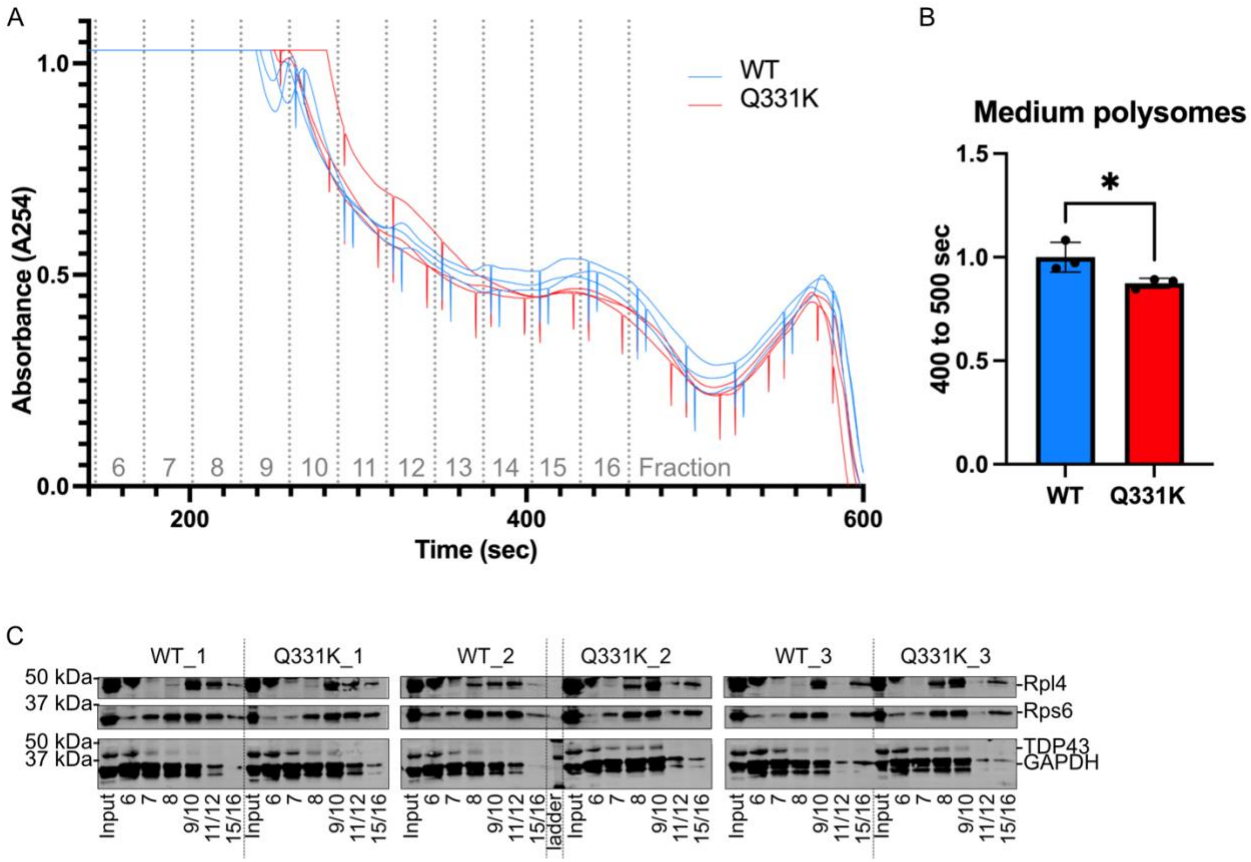

D

Sample	28S/18S	RQN
WT_1	1.3	9
Q331K_1	1.2	9.2
WT_2	1.3	9
Q331K_2	1.4	9.1
WT_3	1.0	7.9
Q331K_3	0.9	6.0

Figure S11. Polysome profiling of cytoplasmic fractions confirm the presence of intact ribosomes. **(A)** Graph of sucrose gradient fractions post-ultracentrifugation. The prominent peaks are at fractions 9/10, fractions 11/12, and fractions 15/16. **(B)** The area under the curve was calculated for all samples at 400 sec to 500 sec to estimate relative amount of medium polysomes, as this was the only ribosomal peak consistently observed in all samples. * = p-value <0.05. **(C)** Western analyses of the protein precipitated fractions of the polysome profile shown in A. Numbers indicate specific fractions analyzed. **(D)** Fragment analysis of RNA isolated from cytoplasmic fractions for each sample subjected to polysome profiling using the Agilent Fragment Analyzer.

1400 **Additional file 2. FIJI Macro for Per FOV N/C Analysis**. Macro script to be used in
1401 FIJI/ImageJ to complete TDP-43 localization analysis on a per FOV level. DAPI signal is used to
1402 define and separate the nuclear and non-nuclear regions where TDP-43 fluorescent signal is
1403 measured to determine the N/C ratio.
1404
1405 **Additional file 3. CellProfiler Pipeline for Per Cell N/C Ratio and Ring-like Analysis.**
1406 CellProfiler Pipeline used for per cell analyses of TDP-43 fluorescent signal including N/C ratio
1407 and ring-like TDP-43 signal. DAPI signal is used to identify individual cells, as well as define
1408 nuclear and cytoplasmic regions for N/C ratio analyses. For ring-like analysis, the nuclear region
1409 is binned into 3 rings to report on distribution of TDP-43 signal.
1410
1411 **Additional file 4, Supp. Table I. Statistical output of RNAseq analyses**. For all comparisons,
1412 logFC refers to log2(fold change), PValue refers to nominal p-value, and FDR refers to adjusted
1413 p-value. Nominal p-values <0.05 are indicated in orange and FDR < 0.1 in red. (**IA**) Statistical
1414 analyses for the 4 mo old mouse cohorts including the 24 h post-surgery (TBI and sham) and
1415 naïve groups. (**IB**) Statistical analyses for the 7 mo post-surgery cohorts.
1416
1417 **Additional file 5, Supp.Table II. GSEA analyses for all comparisons from the RNAseq**
1418 **analysis**. All gene set hits that passed the cutoff criteria (NES > 1.5, FDR > 0.05) are listed. Each
1419 tab is a unique group comparison. In each tab, the top upregulated gene sets are beneath the
1420 purple-shaded header on the left, while the top downregulated gene sets are beneath the blue-
1421 shaded header on the right. Results of hallmark and GOBP are shown. (**IIA**) List of abbreviations
1422 used in the file. (**IIB-E**) Gene set hits for the 24h-post surgery (TBI and sham). (**IIF**) Gene set hits
1423 for Q331K naïve mice relative to WT naïve mice at 4 months of age. (**IIG-IIJ**) Detailed gene lists
1424 for the top pathway hits for the 24h group comparisons. (**IIK-IIN**) Gene set hits for each group
1425 comparison at 7 mo post-surgery.
1426
1427 **Additional file 6, Supp. Table III. Statistical analyses of whole brain quantitative proteomics**
1428 **from Q331K and WT mice with surgery**. Unadjusted p-values ≤ 0.05 are highlighted red
1429 (columns H-K). Adjusted p-values ≤ 0.1 are highlighted in red (columns L-O). Coef. refers to
1430 Log_2(fold change); P.value indicates nominal p-value; P.value.adj. represents adjusted p-value
1431 (FDR).
1432
1433 **Additional file 7, Supp. Table IV. Overlap of published omics datasets with the current**
1434 **study.** Includes all identified proteome and transcriptome level changes in Q331K relative to WT
1435 mice from the current study. Columns B-D refer to datasets in the present study. RNAseq_Sham
1436 refers to the Q331K sham versus WT sham comparison. RNAseq_Naive refers to Q331K naïve
1437 versus WT naïve at 4 months of age. Proteomics_Sham refers to Q331K sham versus WT sham
1438 whole brain proteomics. Columns E/F refer to results published by White et al.(44).
1439
1440 **Additional file 8, Supp. Table V. RT-PCR primers.** Sequence information for primers that were
1441 used to identify alternative splicing for targets of TDP-43 in **Figures 5** and **S8**.
1442
1443 **Additional file 9, Supp. Table VI. Significant outcomes from quantitative proteomics on**
1444 **organelle-depleted cytoplasmic brain lysates.** (**VIIA**) PISA quantitative proteomics results.
1445 (**VIIB**) Traditional quantitative proteomics results (i.e. not exposed to heat). Unadjusted p-values
1446 ≤ 0.05 are highlighted red (columns K-Q). Adjusted p-values ≤ 0.1 are highlighted in red (columns
1447 R-X). Coef. refers to Log_2(fold change); P.value indicates nominal p-value; P.value.adj.
1448 represents adjusted p-value (FDR).
1449

1450 **Additional file 10, Supp. Table VII. GSEA analyses of quantitative proteomics outcomes for**
1451 **organelle-depleted cytoplasmic brain lysates.** All gene set hits that passed the cutoff criteria
1452 (NES > 1.5, FDR > 0.05) are listed. Each tab is a unique group comparison. In each tab, the top
1453 upregulated gene sets are beneath the purple-shaded header on the left, while the top
1454 downregulated gene sets are beneath the blue-shaded header on the right. Results of hallmark
1455 and GOBP are shown. (**VIIIA-D**) Gene set hits for samples processed using PISA. (**VIIIE-H**) Gene
1456 set hits from the traditional quantitative proteomics analyses.
1457

1458 **References**

1459 1. Buratti E, Baralle FE. Multiple roles of TDP-43 in gene expression, splicing regulation,
1460 and human disease. Front Biosci. 2008;13:867-78.

1461 2. Dewey CM, Cenik B, Sephton CF, Dries DR, Mayer P, 3rd, Good SK, et al. TDP-43 is
1462 directed to stress granules by sorbitol, a novel physiological osmotic and oxidative stressor.
1463 Molecular and cellular biology. 2010.

1464 3. Duan L, Zaepfel BL, Aksenova V, Dasso M, Rothstein JD, Kalab P, et al. Nuclear RNA
1465 binding regulates TDP-43 nuclear localization and passive nuclear export. Cell Rep.
1466 2022;40(3):111106.

1467 4. Klim JR, Williams LA, Limone F, Guerra San Juan I, Davis-Dusenbery BN, Mordes DA,
1468 et al. ALS-implicated protein TDP-43 sustains levels of STMN2, a mediator of motor neuron
1469 growth and repair. Nat Neurosci. 2019;22(2):167-79.

1470 5. Tischbein M, Baron DM, Lin YC, Gall KV, Landers JE, Fallini C, et al. The RNA-binding
1471 protein FUS/TLS undergoes calcium-mediated nuclear egress during excitotoxic stress and is
1472 required for GRIA2 mRNA processing. J Biol Chem. 2019;294(26):10194-210.

1473 6. Weskamp K, Tank EM, Miguez R, McBride JP, Gomez NB, White M, et al. Shortened
1474 TDP43 isoforms upregulated by neuronal hyperactivity drive TDP43 pathology in ALS. J Clin
1475 Invest. 2020;130(3):1139-55.

1476 7. Perez-Berlanga M, Wiersma VI, Zbinden A, De Vos L, Wagner U, Foglieni C, et al. Loss
1477 of TDP-43 oligomerization or RNA binding elicits distinct aggregation patterns. EMBO J.
1478 2023;42(17):e111719.

1479 8. Zhang S, Vazquez-Sanchez S, Lu S, Baughn MW, Lim J, Oung S, et al. Acetylation of
1480 lysine 82 initiates TDP-43 nuclear loss of function by disrupting its nuclear import. bioRxiv.
1481 2024:2024.09.04.611121.

1482 9. Necarsulmer JC, Simon JM, Evangelista BA, Chen Y, Tian X, Nafees S, et al. RNA-
1483 binding deficient TDP-43 drives cognitive decline in a mouse model of TDP-43 proteinopathy.
1484 Elife. 2023;12.

1485 10. Dos Passos PM, Hemamali EH, Mamede LD, Hayes LR, Ayala YM. RNA-mediated
1486 ribonucleoprotein assembly controls TDP-43 nuclear retention. PLoS Biol.
1487 2024;22(2):e3002527.

1488 11. Liu-Yesucevitz L, Bilgutay A, Zhang YJ, Vanderwyde T, Citro A, Mehta T, et al. Tar DNA
1489 binding protein-43 (TDP-43) associates with stress granules: analysis of cultured cells and
1490 pathological brain tissue. PloS one. 2010;5(10):e13250.

1491 12. McDonald KK, Aulas A, Destroismaisons L, Pickles S, Beleac E, Camu W, et al. TAR
1492 DNA-binding protein 43 (TDP-43) regulates stress granule dynamics via differential regulation of
1493 G3BP and TIA-1. Human molecular genetics. 2011.

1494 13. Anderson EN, Gochenaur L, Singh A, Grant R, Patel K, Watkins S, et al. Traumatic
1495 injury induces Stress Granule Formation and enhances Motor Dysfunctions in ALS/FTD Models.
1496 Human molecular genetics. 2018.

1497 14. Alami NH, Smith RB, Carrasco MA, Williams LA, Winborn CS, Han SSW, et al. Axonal
1498 transport of TDP-43 mRNA granules is impaired by ALS-causing mutations. Neuron.
1499 2014;81(3):536-43.
1500 15. Dubinski A, Gagne M, Peyrard S, Gordon D, Talbot K, Vande Velde C. Stress granule
1501 assembly in vivo is deficient in the CNS of mutant TDP-43 ALS mice. Human molecular
1502 genetics. 2023;32(2):319-32.
1503 16. Gopal PP, Nirschl JJ, Klinman E, Holzbaur EL. Amyotrophic lateral sclerosis-linked
1504 mutations increase the viscosity of liquid-like TDP-43 RNP granules in neurons. Proc Natl Acad
1505 Sci U S A. 2017;114(12):E2466-E75.
1506 17. Conicella AE, Zerze GH, Mittal J, Fawzi NL. ALS Mutations Disrupt Phase Separation
1507 Mediated by alpha-Helical Structure in the TDP-43 Low-Complexity C-Terminal Domain.
1508 Structure. 2016;24(9):1537-49.
1509 18. Gao J, Wang L, Ren X, Dunn JR, Peters A, Miyagi M, et al. Translational regulation in
1510 the brain by TDP-43 phase separation. J Cell Biol. 2021;220(10).
1511 19. Hallegger M, Chakrabarti AM, Lee FCY, Lee BL, Amalietti AG, Odeh HM, et al. TDP-43
1512 condensation properties specify its RNA-binding and regulatory repertoire. Cell.
1513 2021;184(18):4680-96 e22.
1514 20. Grese ZR, Bastos AC, Mamede LD, French RL, Miller TM, Ayala YM. Specific RNA
1515 interactions promote TDP-43 multivalent phase separation and maintain liquid properties.
1516 EMBO Rep. 2021;22(12):e53632.
1517 21. de Boer EMJ, Orie VK, Williams T, Baker MR, De Oliveira HM, Polvikoski T, et al. TDP-
1518 43 proteinopathies: a new wave of neurodegenerative diseases. J Neurol Neurosurg Psychiatry.
1519 2020;92(1):86-95.
1520 22. Arai T, Hasegawa M, Akiyama H, Ikeda K, Nonaka T, Mori H, et al. TDP-43 is a
1521 component of ubiquitin-positive tau-negative inclusions in frontotemporal lobar degeneration
1522 and amyotrophic lateral sclerosis. Biochem Biophys Res Commun. 2006;351(3):602-11.
1523 23. Neumann M, Sampathu DM, Kwong LK, Truax AC, Micsenyi MC, Chou TT, et al.
1524 Ubiquitinated TDP-43 in frontotemporal lobar degeneration and amyotrophic lateral sclerosis.
1525 Science. 2006;314(5796):130-3.
1526 24. Amador-Ortiz C, Lin WL, Ahmed Z, Personett D, Davies P, Duara R, et al. TDP-43
1527 immunoreactivity in hippocampal sclerosis and Alzheimer's disease. Ann Neurol.
1528 2007;61(5):435-45.
1529 25. Nelson PT, Dickson DW, Trojanowski JQ, Jack CR, Boyle PA, Arfanakis K, et al. Limbic-
1530 predominant age-related TDP-43 encephalopathy (LATE): consensus working group report.
1531 Brain. 2019;142(6):1503-27.
1532 26. McKee AC, Gavett BE, Stern RA, Nowinski CJ, Cantu RC, Kowall NW, et al. TDP-43
1533 proteinopathy and motor neuron disease in chronic traumatic encephalopathy. J Neuropathol
1534 Exp Neurol. 2010;69(9):918-29.
1535 27. Brown AL, Wilkins OG, Keuss MJ, Hill SE, Zanovello M, Lee WC, et al. TDP-43 loss and
1536 ALS-risk SNPs drive mis-splicing and depletion of UNC13A. Nature. 2022;603(7899):131-7.
1537 28. Estades Ayuso V, Pickles S, Todd T, Yue M, Jansen-West K, Song Y, et al. TDP-43-
1538 regulated cryptic RNAs accumulate in Alzheimer's disease brains. Mol Neurodegener.
1539 2023;18(1):57.
1540 29. Ling JP, Pletnikova O, Troncoso JC, Wong PC. TDP-43 repression of nonconserved
1541 cryptic exons is compromised in ALS-FTD. Science. 2015;349(6248):650-5.

1542 30. Ma XR, Prudencio M, Koike Y, Vatsavayai SC, Kim G, Harbinski F, et al. TDP-43
1543 represses cryptic exon inclusion in the FTD-ALS gene UNC13A. Nature. 2022;603(7899):124-
1544 30.
1545 31. Melamed Z, Lopez-Erauskin J, Baughn MW, Zhang O, Drenner K, Sun Y, et al.
1546 Premature polyadenylation-mediated loss of stathmin-2 is a hallmark of TDP-43-dependent
1547 neurodegeneration. Nat Neurosci. 2019;22(2):180-90.
1548 32. Al-Chalabi A, Hardiman O. The epidemiology of ALS: a conspiracy of genes,
1549 environment and time. Nat Rev Neurol. 2013;9(11):617-28.
1550 33. Goutman SA, Savelieff MG, Jang DG, Hur J, Feldman EL. The amyotrophic lateral
1551 sclerosis exposome: recent advances and future directions. Nat Rev Neurol. 2023;19(10):617-
1552 34.
1553 34. Chio A, Mazzini L, D'Alfonso S, Corrado L, Canosa A, Moglia C, et al. The multistep
1554 hypothesis of ALS revisited: The role of genetic mutations. Neurology. 2018;91(7):e635-e42.
1555 35. Al-Chalabi A, Calvo A, Chio A, Colville S, Ellis CM, Hardiman O, et al. Analysis of
1556 amyotrophic lateral sclerosis as a multistep process: a population-based modelling study.
1557 Lancet Neurol. 2014;13(11):1108-13.
1558 36. Barker S, Paul BD, Pieper AA. Increased Risk of Aging-Related Neurodegenerative
1559 Disease after Traumatic Brain Injury. Biomedicines. 2023;11(4).
1560 37. Heyburn L, Sajja V, Long JB. The Role of TDP-43 in Military-Relevant TBI and Chronic
1561 Neurodegeneration. Front Neurol. 2019;10:680.
1562 38. Jankovic T, Dolenec P, Rajic Bumber J, Grzeta N, Kriz J, Zupan G, et al. Differential
1563 Expression Patterns of TDP-43 in Single Moderate versus Repetitive Mild Traumatic Brain Injury
1564 in Mice. Int J Mol Sci. 2021;22(22).
1565 39. Kahriman A, Bouley J, Smith TW, Bosco DA, Woerman AL, Henninger N. Mouse closed
1566 head traumatic brain injury replicates the histological tau pathology pattern of human disease:
1567 characterization of a novel model and systematic review of the literature. Acta Neuropathol
1568 Commun. 2021;9(1):118.
1569 40. Kahriman A, Bouley J, Tuncali I, Dogan EO, Pereira M, Luu T, et al. Repeated mild
1570 traumatic brain injury triggers pathology in asymptomatic C9ORF72 transgenic mice. Brain.
1571 2023;146(12):5139-52.
1572 41. Wiesner D, Tar L, Linkus B, Chandrasekar A, Olde Heuvel F, Dupuis L, et al. Reversible
1573 induction of TDP-43 granules in cortical neurons after traumatic injury. Exp Neurol. 2018;299(Pt
1574 A):15-25.
1575 42. Stein TD, Alvarez VE, McKee AC. Chronic traumatic encephalopathy: a spectrum of
1576 neuropathological changes following repetitive brain trauma in athletes and military personnel.
1577 Alzheimers Res Ther. 2014;6(1):4.
1578 43. Henninger N, Bouley J, Sikoglu EM, An J, Moore CM, King JA, et al. Attenuated
1579 traumatic axonal injury and improved functional outcome after traumatic brain injury in mice
1580 lacking Sarm1. Brain. 2016;139(Pt 4):1094-105.
1581 44. White MA, Kim E, Duffy A, Adalbert R, Phillips BU, Peters OM, et al. TDP-43 gains
1582 function due to perturbed autoregulation in a Tardbp knock-in mouse model of ALS-FTD. Nat
1583 Neurosci. 2018;21(4):552-63.
1584 45. Hasan R, Humphrey J, Bettencourt C, Newcombe J, Consortium NA, Lashley T, et al.
1585 Transcriptomic analysis of frontotemporal lobar degeneration with TDP-43 pathology reveals
1586 cellular alterations across multiple brain regions. Acta Neuropathol. 2022;143(3):383-401.

1587 46. Humphrey J, Venkatesh S, Hasan R, Herb JT, de Paiva Lopes K, Kucukali F, et al.
1588 Integrative transcriptomic analysis of the amyotrophic lateral sclerosis spinal cord implicates
1589 glial activation and suggests new risk genes. Nat Neurosci. 2023;26(1):150-62.

1590 47. Neelagandan N, Gonnella G, Dang S, Janiesch PC, Miller KK, Kuchler K, et al. TDP-43
1591 enhances translation of specific mRNAs linked to neurodegenerative disease. Nucleic Acids
1592 Res. 2019;47(1):341-61.

1593 48. Russo A, Scardigli R, La Regina F, Murray ME, Romano N, Dickson DW, et al.
1594 Increased cytoplasmic TDP-43 reduces global protein synthesis by interacting with RACK1 on
1595 polyribosomes. Human molecular genetics. 2017;26(8):1407-18.

1596 49. Bjork RT, Mortimore NP, Loganathan S, Zarnescu DC. Dysregulation of Translation in
1597 TDP-43 Proteinopathies: Deficits in the RNA Supply Chain and Local Protein Production. Front
1598 Neurosci. 2022;16:840357.

1599 50. Piol D, Robberechts T, Da Cruz S. Lost in local translation: TDP-43 and FUS in
1600 axonal/neuromuscular junction maintenance and dysregulation in amyotrophic lateral sclerosis.
1601 Neuron. 2023;111(9):1355-80.

1602 51. Zhong J, Gunner G, Henninger N, Schafer DP, Bosco DA. Intravital Imaging of
1603 Fluorescent Protein Expression in Mice with a Closed-Skull Traumatic Brain Injury and Cranial
1604 Window Using a Two-Photon Microscope. J Vis Exp. 2023(194).

1605 52. Dogan EO, Bouley J, Zhong J, Harkins AL, Keeler AM, Bosco DA, et al. Genetic ablation
1606 of Sarm1 attenuates expression and mislocalization of phosphorylated TDP-43 after mouse
1607 repetitive traumatic brain injury. Acta Neuropathol Commun. 2023;11(1):206.

1608 53. Flierl MA, Stahel PF, Beauchamp KM, Morgan SJ, Smith WR, Shohami E. Mouse closed
1609 head injury model induced by a weight-drop device. Nat Protoc. 2009;4(9):1328-37.

1610 54. Kim D, Paggi JM, Park C, Bennett C, Salzberg SL. Graph-based genome alignment and
1611 genotyping with HISAT2 and HISAT-genotype. Nat Biotechnol. 2019;37(8):907-15.

1612 55. Chen Y, Lun AT, Smyth GK. From reads to genes to pathways: differential expression
1613 analysis of RNA-Seq experiments using Rsubread and the edgeR quasi-likelihood pipeline.
1614 F1000Res. 2016;5:1438.

1615 56. Castanza AS, Recla JM, Eby D, Thorvaldsdottir H, Bult CJ, Mesirov JP. Extending
1616 support for mouse data in the Molecular Signatures Database (MSigDB). Nat Methods.
1617 2023;20(11):1619-20.

1618 57. Liberzon A, Birger C, Thorvaldsdottir H, Ghandi M, Mesirov JP, Tamayo P. The
1619 Molecular Signatures Database (MSigDB) hallmark gene set collection. Cell Syst.
1620 2015;1(6):417-25.

1621 58. Liberzon A, Subramanian A, Pinchback R, Thorvaldsdottir H, Tamayo P, Mesirov JP.
1622 Molecular signatures database (MSigDB) 3.0. Bioinformatics. 2011;27(12):1739-40.

1623 59. Mootha VK, Lindgren CM, Eriksson KF, Subramanian A, Sihag S, Lehar J, et al. PGC-
1624 1alpha-responsive genes involved in oxidative phosphorylation are coordinately downregulated
1625 in human diabetes. Nat Genet. 2003;34(3):267-73.

1626 60. Subramanian A, Tamayo P, Mootha VK, Mukherjee S, Ebert BL, Gillette MA, et al. Gene
1627 set enrichment analysis: a knowledge-based approach for interpreting genome-wide expression
1628 profiles. Proc Natl Acad Sci U S A. 2005;102(43):15545-50.

1629 61. Funes S, Jung J, Gadd DH, Mosqueda M, Zhong J, Shankaracharya, et al. Expression
1630 of ALS-PFN1 impairs vesicular degradation in iPSC-derived microglia. Nat Commun.
1631 2024;15(1):2497.

1632 62. Tyanova S, Temu T, Cox J. The MaxQuant computational platform for mass
1633 spectrometry-based shotgun proteomics. Nat Protoc. 2016;11(12):2301-19.

1634 63. Tyanova S, Temu T, Sinitcyn P, Carlson A, Hein MY, Geiger T, et al. The Perseus
1635 computational platform for comprehensive analysis of (prote)omics data. Nat Methods.
1636 2016;13(9):731-40.
1637 64. Schindelin J, Arganda-Carreras I, Frise E, Kaynig V, Longair M, Pietzsch T, et al. Fiji: an
1638 open-source platform for biological-image analysis. Nat Methods. 2012;9(7):676-82.
1639 65. Kamentsky L, Jones TR, Fraser A, Bray MA, Logan DJ, Madden KL, et al. Improved
1640 structure, function and compatibility for CellProfiler: modular high-throughput image analysis
1641 software. Bioinformatics. 2011;27(8):1179-80.
1642 66. Jumper J, Evans R, Pritzel A, Green T, Figurnov M, Ronneberger O, et al. Highly
1643 accurate protein structure prediction with AlphaFold. Nature. 2021;596(7873):583-9.
1644 67. Darnell JC, Van Driesche SJ, Zhang C, Hung KY, Mele A, Fraser CE, et al. FMRP stalls
1645 ribosomal translocation on mRNAs linked to synaptic function and autism. Cell.
1646 2011;146(2):247-61.
1647 68. Dogan EO, Simonini SR, Bouley J, Weiss A, Brown RH, Jr., Henninger N. Genetic
1648 Ablation of Sarm1 Mitigates Disease Acceleration after Traumatic Brain Injury in the
1649 SOD1(G93A) Transgenic Mouse Model of Amyotrophic Lateral Sclerosis. Ann Neurol. 2025.
1650 69. Curzon P, Rustay NR, Browman KE. Cued and Contextual Fear Conditioning for
1651 Rodents. 2nd ed: CRC Press/Taylor & Francis, Boca Raton (FL); 2009 2009.
1652 70. Maren S, Quirk GJ. Neuronal signalling of fear memory. Nat Rev Neurosci.
1653 2004;5(11):844-52.
1654 71. Querfurth H, Lee HK. Mammalian/mechanistic target of rapamycin (mTOR) complexes in
1655 neurodegeneration. Mol Neurodegener. 2021;16(1):44.
1656 72. Simon DW, McGeachy MJ, Bayir H, Clark RS, Loane DJ, Kochanek PM. The far-
1657 reaching scope of neuroinflammation after traumatic brain injury. Nat Rev Neurol.
1658 2017;13(3):171-91.
1659 73. Hubbard WB, Joseph B, Spry M, Vekaria HJ, Saatman KE, Sullivan PG. Acute
1660 Mitochondrial Impairment Underlies Prolonged Cellular Dysfunction after Repeated Mild
1661 Traumatic Brain Injuries. J Neurotrauma. 2019;36(8):1252-63.
1662 74. Wang W, Wang L, Lu J, Siedlak SL, Fujioka H, Liang J, et al. The inhibition of TDP-43
1663 mitochondrial localization blocks its neuronal toxicity. Nat Med. 2016;22(8):869-78.
1664 75. Yoshida H, Matsui T, Yamamoto A, Okada T, Mori K. XBP1 mRNA is induced by ATF6
1665 and spliced by IRE1 in response to ER stress to produce a highly active transcription factor.
1666 Cell. 2001;107(7):881-91.
1667 76. Pineda SS, Lee H, Ulloa-Navas MJ, Linville RM, Garcia FJ, Galani K, et al. Single-cell
1668 dissection of the human motor and prefrontal cortices in ALS and FTLD. Cell.
1669 2024;187(8):1971-89 e16.
1670 77. Perucho L, Artero-Castro A, Guerrero S, Ramon y Cajal S, ME LL, Wang ZQ. RPLP1, a
1671 crucial ribosomal protein for embryonic development of the nervous system. PLoS One.
1672 2014;9(6):e99956.
1673 78. Moisse K, Volkening K, Leystra-Lantz C, Welch I, Hill T, Strong MJ. Divergent patterns
1674 of cytosolic TDP-43 and neuronal progranulin expression following axotomy: implications for
1675 TDP-43 in the physiological response to neuronal injury. Brain Res. 2009;1249:202-11.
1676 79. Mehta PR, Brown AL, Ward ME, Fratta P. The era of cryptic exons: implications for ALS-
1677 FTD. Mol Neurodegener. 2023;18(1):16.
1678 80. Rouaux C, Gonzalez De Aguilar JL, Dupuis L. Unmasking the skiptic task of TDP-43.
1679 EMBO J. 2018;37(11).

1680 81. Arnold ES, Ling SC, Huelga SC, Lagier-Tourenne C, Polymenidou M, Ditsworth D, et al.
1681 ALS-linked TDP-43 mutations produce aberrant RNA splicing and adult-onset motor neuron
1682 disease without aggregation or loss of nuclear TDP-43. Proc Natl Acad Sci U S A.
1683 2013;110(8):E736-45.

1684 82. Fratta P, Sivakumar P, Humphrey J, Lo K, Ricketts T, Oliveira H, et al. Mice with
1685 endogenous TDP-43 mutations exhibit gain of splicing function and characteristics of
1686 amyotrophic lateral sclerosis. EMBO J. 2018;37(11).

1687 83. Polymenidou M, Lagier-Tourenne C, Hutt KR, Huelga SC, Moran J, Liang TY, et al. Long
1688 pre-mRNA depletion and RNA missplicing contribute to neuronal vulnerability from loss of TDP-
1689 43. Nat Neurosci. 2011;14(4):459-68.

1690 84. Yang C, Qiao T, Yu J, Wang H, Guo Y, Salameh J, et al. Low-level overexpression of
1691 wild type TDP-43 causes late-onset, progressive neurodegeneration and paralysis in mice.
1692 PLoS One. 2022;17(2):e0255710.

1693 85. Chu BW, Kovary KM, Guillaume J, Chen LC, Teruel MN, Wandless TJ. The E3 ubiquitin
1694 ligase UBE3C enhances proteasome processivity by ubiquitinating partially proteolyzed
1695 substrates. J Biol Chem. 2013;288(48):34575-87.

1696 86. Gaetani M, Zubarev RA. Proteome Integral Solubility Alteration (PISA) for High-
1697 Throughput Ligand Target Deconvolution with Increased Statistical Significance and Reduced
1698 Sample Amount. Methods Mol Biol. 2023;2554:91-106.

1699 87. Li J, Van Vranken JG, Paulo JA, Huttlin EL, Gygi SP. Selection of Heating Temperatures
1700 Improves the Sensitivity of the Proteome Integral Solubility Alteration Assay. J Proteome Res.
1701 2020;19(5):2159-66.

1702 88. Savitski MM, Reinhard FB, Franken H, Werner T, Savitski MF, Eberhard D, et al.
1703 Tracking cancer drugs in living cells by thermal profiling of the proteome. Science.
1704 2014;346(6205):1255784.

1705 89. Brohee S, van Helden J. Evaluation of clustering algorithms for protein-protein
1706 interaction networks. BMC Bioinformatics. 2006;7:488.

1707 90. Szklarczyk D, Kirsch R, Koutrouli M, Nastou K, Mehryary F, Hachilif R, et al. The
1708 STRING database in 2023: protein-protein association networks and functional enrichment
1709 analyses for any sequenced genome of interest. Nucleic Acids Res. 2023;51(D1):D638-D46.

1710 91. Cheng F, Chapman T, Venturato J, Davidson JM, Polido SA, Rosa-Fernandes L, et al.
1711 Proteomics Analysis of the TDP-43 Interactome in Cellular Models of ALS Pathogenesis. J
1712 Neurochem. 2025;169(5):e70079.

1713 92. Freibaum BD, Chitta RK, High AA, Taylor JP. Global analysis of TDP-43 interacting
1714 proteins reveals strong association with RNA splicing and translation machinery. J Proteome
1715 Res. 2010;9(2):1104-20.

1716 93. Zeng C, Han S, Pan Y, Huang Z, Zhang B, Zhang B. Revisiting the chaperonin T-
1717 complex protein-1 ring complex in human health and disease: A proteostasis modulator and
1718 beyond. Clin Transl Med. 2024;14(2):e1592.

1719 94. Luo J, Zhao H, Chen L, Liu M. Multifaceted functions of RPS27a: An unconventional
1720 ribosomal protein. J Cell Physiol. 2023;238(3):485-97.

1721 95. Lin Z, Kim E, Ahmed M, Han G, Simmons C, Redhead Y, et al. MRI-guided histology of
1722 TDP-43 knock-in mice implicates parvalbumin interneuron loss, impaired neurogenesis and
1723 aberrant neurodevelopment in amyotrophic lateral sclerosis-frontotemporal dementia. Brain
1724 Commun. 2021;3(2):fcab114.

1725 96. Kelmer Sacramento E, Kirkpatrick JM, Mazzetto M, Baumgart M, Bartolome A, Di Sanzo
1726 S, et al. Reduced proteasome activity in the aging brain results in ribosome stoichiometry loss
1727 and aggregation. Mol Syst Biol. 2020;16(6):e9596.
1728 97. Amirbeigiarab S, Kiani P, Velazquez Sanchez A, Krisp C, Kazantsev A, Fester L, et al.
1729 Invariable stoichiometry of ribosomal proteins in mouse brain tissues with aging. Proc Natl Acad
1730 Sci U S A. 2019;116(45):22567-72.
1731 98. Zhao B, Cowan CM, Coutts JA, Christy DD, Saraph A, Hsueh SCC, et al. Targeting
1732 RACK1 to alleviate TDP-43 and FUS proteinopathy-mediated suppression of protein translation
1733 and neurodegeneration. Acta Neuropathol Commun. 2023;11(1):200.
1734 99. Bhavsar RB, Makley LN, Tsonis PA. The other lives of ribosomal proteins. Hum
1735 Genomics. 2010;4(5):327-44.
1736 100. Simsek D, Barna M. An emerging role for the ribosome as a nexus for post-translational
1737 modifications. Curr Opin Cell Biol. 2017;45:92-101.
1738 101. Ali A, Garde R, Schaffer OC, Bard JAM, Husain K, Kik SK, et al. Adaptive preservation
1739 of orphan ribosomal proteins in chaperone-dispersed condensates. Nat Cell Biol.
1740 2023;25(11):1691-703.
1741 102. Nagano S, Jinno J, Abdelhamid RF, Jin Y, Shibata M, Watanabe S, et al. TDP-43
1742 transports ribosomal protein mRNA to regulate axonal local translation in neuronal axons. Acta
1743 Neuropathol. 2020;140(5):695-713.
1744 103. Tank EM, Figueroa-Romero C, Hinder LM, Bedi K, Archbold HC, Li X, et al. Abnormal
1745 RNA stability in amyotrophic lateral sclerosis. Nat Commun. 2018;9(1):2845.
1746 104. Chou A, Krukowski K, Jopson T, Zhu PJ, Costa-Mattioli M, Walter P, et al. Inhibition of
1747 the integrated stress response reverses cognitive deficits after traumatic brain injury. Proc Natl
1748 Acad Sci U S A. 2017;114(31):E6420-E6.
1749 105. Huang WP, Ellis BCS, Hodgson RE, Sanchez Avila A, Kumar V, Rayment J, et al.
1750 Stress-induced TDP-43 nuclear condensation causes splicing loss of function and STMN2
1751 depletion. Cell Rep. 2024;43(7):114421.
1752 106. Rifai OM, Waldron FM, O'Shaughnessy J, Read FL, Gilodi M, Pastore A, et al. Amygdala
1753 TDP-43 pathology is associated with behavioural dysfunction and ferritin accumulation in
1754 amyotrophic lateral sclerosis. bioRxiv. 2024.
1755 107. Wilkins OG, Chien M, Wlaschin JJ, Barattucci S, Harley P, Mattedi F, et al. Creation of
1756 de novo cryptic splicing for ALS and FTD precision medicine. Science. 2024;386(6717):61-9.
1757 108. Francois-Moutal L, Perez-Miller S, Scott DD, Miranda VG, Mollasalehi N, Khanna M.
1758 Structural Insights Into TDP-43 and Effects of Post-translational Modifications. Front Mol
1759 Neurosci. 2019;12:301.
1760 109. Shenouda M, Xiao S, MacNair L, Lau A, Robertson J. A C-Terminally Truncated TDP-43
1761 Splice Isoform Exhibits Neuronal Specific Cytoplasmic Aggregation and Contributes to TDP-43
1762 Pathology in ALS. Front Neurosci. 2022;16:868556.
1763 110. Elliott E, Bailey O, Waldron FM, Hardingham GE, Chandran S, Gregory JM. Therapeutic
1764 Targeting of Proteostasis in Amyotrophic Lateral Sclerosis-a Systematic Review and Meta-
1765 Analysis of Preclinical Research. Front Neurosci. 2020;14:511.
1766